Improved Kinetics for Mineral Dissolution Reactions in Pore-Scale Reactive Transport Modeling

Schabernack, J.; Fischer, C.;

Originally published:

August 2022

Geochimica et Cosmochimica Acta 334(2022), 99-118

DOI: https://doi.org/10.1016/j.gca.2022.08.003

Perma-Link to Publication Repository of HZDR:

https://www.hzdr.de/publications/Publ-34374

Improved Kinetics for Mineral Dissolution Reactions in Pore-Scale Reactive Transport Modeling

Jonas Schabernack[a]*, Cornelius Fischer[a]

[a]Helmholtz-Zentrum Dresden-Rossendorf, Institute of Resource Ecology, Department of Reactive Transport, D-04318 Leipzig, Permoserstr. 15, Germany

*Corresponding author: Jonas Schabernack
E-Mail address: *j.schabernack@hzdr.de, c.fischer@hzdr.de

Abstract

Recent numerical investigations revealed that the heterogeneity of the dissolution rate observed in numerous experiments cannot be explained by fluid transport effects. This heterogeneity is attributed to intrinsic surface reactivity. Therefore, reactive transport models (RTM) require parameterization of the surface reactivity for accurate predictions. For this purpose, a nanotopographic parametrization based on surface slope has been recently suggested. In this study, we utilize and improve this parametrization for RTMs of pore-scale systems, from the crystal surface to the single crystal geometry, going beyond the previous reactivity parametrization. 2D and 3D RTMs were developed using COMSOL Multiphysics for calcite systems based on experimental measurements. We compared the results between classically parameterized RTMs, RTMs with new slope parameterization, and experimental data. The effect of flow on dissolution under conditions far-from-equilibrium is found to be negligible, highlighting the importance of surface reactivity in the dissolution reaction. For the first time, the new slope factor was able to accurately reproduce the experimental results on a crystal surface with large field-of-view, large height variability of the topography, and over a long-term reaction period. The new parameterization had greatly improved sensitivity for intermediate reactivity ranges compared to the previous parameterization. A 3D model is used to present the general applicability of the parameterization for use in realistic geometric data sets. Thus, we also show that neglecting surface reactivity in an RTM leads to incorrect predictions regarding the porosity, pore geometry, and surface topography of the system. Our new slope factor can successfully serve as a first-order proxy for the distribution of surface reactivity in 3D pore-scale rock systems. The description of surface reactivity is crucial for accurate long-term modeling of natural rock systems.

Keywords

Pore-Scale Reactive Transport Modeling; Mineral Dissolution; Crystal Surface Reactivity; Kinetics

1. Introduction

Mineral dissolution plays a key role in various natural processes such as weathering or reservoir rock formation, as well as in technical applications such as corrosion, mining, and waste management. Predicting mineral dissolution over long timescales (>100,000 years) is crucial to describe the stability of geomaterials in important applications, e.g., nuclear waste repositories for underground storage (Ewing et al., 2016). Such predictions require a detailed understanding of the mechanistic processes involved in the dissolution reactions. An adequate model parametrization based on mechanistic insight is required to simulate the long-term behavior of any given system.

Mineral dissolution is typically quantified via a dissolution rate. In the past, bulk-powder experiments have been applied to study the dissolution of various minerals (e.g., Chou et al., 1989; Plummer et al., 1978). In these experiments, a single, mineral-specific value for dissolution rate is determined. However, the reported individual dissolution rates for the same mineral, similar fluid compositions, and experimental conditions can vary by several orders of magnitude (Arvidson et al., 2003; Bollermann and Fischer, 2020). Surface-sensitive microscopy techniques such as atomic force microscopy (AFM) (Lange et al., 2021; Pollet-Villard et al., 2016) or vertical scanning interferometry (VSI) (Bouissonnié et al., 2018; Fischer et al., 2012) can directly observe mineral surfaces during dissolution and reveal the evolution of surface topography over time. Tomographic measurements of dissolving materials can be obtained using techniques such as X-ray microtomography (µ-CT) (Noiriel and Soulaine, 2021; Noiriel et al., 2020). The use of these surface-sensitive methods revealed a large intrinsic variability in surface dissolution rates under identical conditions, besides the well-known extrinsic variability (e.g., Noiriel and Daval, 2017; Saldi et al., 2017).

Mineral surface reactivity is not a material constant but arises due to nano- and microstructural heterogeneities caused by 2D and 3D defects in the crystal lattice. The heterogeneous distribution of surface reactivity has been extensively investigated for calcite (Arvidson et al., 2003; Liang and Baer, 1997), and a recent compilation can be found in Bollermann and Fischer (2020). New aspects include inherited reactivity of nanostructured surfaces (Fischer et al., 2018) as well as temporal fluctuations at far-from-equilibrium conditions (Fischer and Luttge, 2018). Similar studies exist for a variety of minerals such as feldspars (Lange et al., 2021; Pollet-Villard et al., 2016; Zhang and Lüttge, 2009), quartz (Kurganskaya and Luttge, 2013), and sheet silicates (Kurganskaya et al., 2012). The lattice defects result in the formation of steps and etch pits on the

crystal surface during reactions. Due to the resulting nanotopography, atomic surface sites with varying coordination and consequently different intrinsic reactivity such as terrace, step, or kink atoms are present on the crystal surface. The local surface reactivity is determined by the concentration of highly reactive kink sites on the crystal surface, according to findings from experimental and numerical investigations (Arvidson et al., 2003; Chen et al., 2014; Fischer et al., 2014). A high concentration of kink sites is typically found at etch pits, surface steps, and crystal corners. Thus, a single dissolution rate cannot adequately describe the complex dissolution kinetics at the crystal surface. Even on larger length scales, the variability in surface reactivity does not average out. This has been shown for both large crystals with edges, corners, faces (Noiriel et al., 2020; Noiriel et al., 2019) as well as polycrystalline materials (Bollermann and Fischer, 2020; Kahl et al., 2020). Powder samples consisting of small crystals typically do not show 2D or 3D lattice defects and exhibit a homogeneous crystal surface consisting almost entirely of kink and step sites with high reactivity (Bollermann and Fischer, 2020). Therefore, predictive approaches for mineral dissolution must consider and implement the distribution and density of reactive surface sites.

In addition to experimental studies on mineral dissolution rates, numerical approaches have been applied to fundamentally understand the mechanisms of dissolution reactions at surfaces. At the nanometer to micrometer scale, kinetic Monte Carlo (KMC) simulations can be applied to study the evolution of surface topography, dissolution rates, and the distribution of surface reactivity as dissolution progresses. KMC can be used to predict dissolution nanotopographies and provides important mechanistic inferences about the dissolution reaction (Kurganskaya and Luttge, 2013). Using this method, it is possible to predict the kink site density and thus the surface reactivity (Kurganskaya and Luttge, 2016). For small crystal sizes, the KMC method can simulate the dissolution of whole crystal grains considering multiple surfaces (Luttge et al., 2013; Martin et al., 2020). Larger system sizes can be achieved by using KMC-parameterized Voronoi simulations, which reduce computational costs while providing similar results (Rohlfs et al., 2018). KMC results can be validated with and compared to experimental data obtained with AFM or VSI measurements, and therefore provide a powerful tool for predicting reaction rates.

At larger scales, reactive transport models (RTM) are commonly applied to simulate fluid flow, species transport and various processes in natural and engineered systems on various scales (Druhan and Tournassat, 2020; Molins et al., 2014; Prasianakis et al., 2017; Shao et al., 2009; Tournassat and Steefel, 2019; Yuan et al., 2016). RTMs can predict the evolution of various chemical and physical system parameters over a wide range of time scales. At the pore scale (µm

scale), the models typically describe the system with two distinct phases: solid and liquid. The model systems consist of pore space available for both fluid flow and transport, and solid mineral grains that interface with the fluid (Molins et al., 2021). Comprehensive reviews of flow and transport modeling are available for porous media (Blunt et al., 2013) and fractures (Berkowitz, 2002).

At the fluid-mineral interface, various interactions such as sorption, dissolution, or precipitation reactions have to be considered depending on the physicochemical conditions in the system. Chemical reactions in RTM are governed by the chemical driving force to reach equilibrium. In the fluid, aqueous complexation occurs as an equilibrium reaction depending on the species in the system (Molins et al., 2014; Steefel et al., 2015). Mineral interfaces dissolve when the fluid is undersaturated in the species of the respective mineral component. In the case of calcite, the main driving force for dissolution is the pH of the liquid, while pCO_2 has only a weak influence (Pokrovsky et al., 2005). The calculation of mineral dissolution in pore-scale RTMs is based on rate laws derived from transition state theory, using rate constants derived from bulk powder experiments (Molins et al., 2014). Thus, the rate calculations are based solely on extrinsic constraints linked via fluid composition.

In contrast, the rate equation does not account for the previously mentioned experimental findings on heterogeneous dissolution rates and intrinsic surface reactivity. This illustrates the limited use of such rate constants for predicting reacting crystalline systems (Karimzadeh and Fischer, 2021). In transport-controlled regimes, the reactant concentrations in the fluid very efficiently control the rate constants describing the reactivity of the processes involved. In surface-controlled conditions, the influence of surface reactivity is by definition more important than transport effects in the system. Therefore, neglecting intrinsic reactivity significantly affects the simulation results and the predictive power of the model. Superimposing the variability of surface reactivity on transport-controlled systems may induce small changes in simulation results since the main influence on dissolution rates originates from concentration gradients in the fluid. In addition to surface reactivity, natural mineral surfaces show distinct nano- to microtopographies arising from heterogeneous dissolution. Therefore, simulations must account for this small-scale interfacial roughness. Recent studies have addressed the influence of roughness in pore-scale RTMs and its effects on transport and mineral dissolution (Deng et al., 2018; Rasoulzadeh et al., 2020; Zou et al., 2017). However, these studies focus on either larger fractures (Zou et al., 2017) or artificially created surface roughness (Deng et al., 2018; Rasoulzadeh et al., 2020). In comparison to measured topographies in dissolution experiments, the height/depth of artificial topography

features is greatly exaggerated, e.g., comparing the roughness used by Deng et al. (2018) with pit depths ≤100 µm to the VSI measurements of Bibi et al. (2018) with depths up to ≤ 2 µm.

Further studies investigated mineral dissolution in 3D µ-CT rock samples and the influence of the flow field on the reaction rate (Menke et al., 2017; Menke et al., 2016). High porosity in the rock formations leads to uniform dissolution, while lower porosities lead to channeling of the flow. The average rock dissolution rate can be orders of magnitude lower than for measurements on flat surface samples. This rate reduction is caused by transport limitations in regions far from fast flow channels and is greatest for channeled flow samples. Numerical simulations based on the µ-CT datasets confirmed the rate reduction for systems with high porosity heterogeneities (Pereira Nunes et al., 2016a; Pereira Nunes et al., 2016b).

A recent study by Agrawal et al. (2021) investigated the effect of hydrodynamics on dissolution rate variability by simulating calcite dissolution based on experimental dissolution rate map data Bollermann and Fischer (2020). Their investigations focused on the heterogeneity of flow owing to increasing surface roughness during dissolution. They showed that local variability of hydrodynamic effects could not explain the experimental dissolution rate distribution. Thus, micrometer-scale heterogeneity of fluid flow field and composition was negligible. The surface roughness in the studied system had no significant hydrodynamic effects on the resulting reaction rates. Overall, the numerical approach failed to reproduce the experimental results, highlighting the need for parameterization of surface reactivity in RTM dissolution rate calculations, especially for surface-controlled conditions. To address this shortcoming, Karimzadeh and Fischer (2021) suggested a surface slope-based parameter, called the surface slope factor (SSF), to serve as a surrogate value for the reactivity distribution. The concept is based on the idea that highly reactive kink sites occur in high concentrations at atomic steps. A high concentration of atomic steps is found at sites with strong height changes in the µm range on the mineral surface, which can be identified with high slope values. Parameterized simulation of a dissolving calcite surface showed good agreement with experimentally obtained dissolution rates.

This study aims to investigate the general applicability of surface slope as a way to parameterize reactivity for improved RTM approaches. The goal is to identify a general pathway to parameterize surface reactivity in pore-scale 3D RTMs, e.g., with µ-CT-derived pore space and mineral grain geometries. For this, we start with the classical pore-scale dissolution RTM approach at far-from-equilibrium conditions using VSI maps of a calcite single crystal (Bibi et al., 2018). This dataset provides a larger field-of-view (FOV) than previous studies on single crystals (Karimzadeh and

Fischer, 2021) or polycrystalline (Agrawal et al., 2021) surfaces. The surface exhibits large height variations on a single crystal surface (up to 2 µm), compared to the surfaces from Karimzadeh and Fischer (2021) with up to 0.1 µm variations. The polycrystalline surfaces of Agrawal et al. (2021) also show up to 2 µm height variation, but the height differences are mainly limited to grain boundaries and do not provide insight into the evolution of large height differences on single crystal surfaces. Additionally, the data set of Bibi et al. (2018) provides surface measurements for a dissolution reaction time of 6 h, which can be used directly for model validation. With these temporal and spatial scale differences, we can test the performance of the SSF parameterization on larger systems and explore a feasible way to upscale the approach to larger 3D systems consisting of multiple crystal grains. To achieve the goal of 3D applicability, we improve the SSF calculation to be independent of the spatial orientation of the surface. In a final step, we apply the slope parameterization approach to a simple 3D artificial rock model and test the influence of surface reactivity on the prediction of mineral dissolution in this system. Overall, this study tests the validity of the SSF parameterization approach for reactivity on a uniquely large data set and aims to provide an upscaling pathway for larger 3D rock pore network geometries.

2. Methods

A classical pore-scale RTM approach was applied to test its predictive capabilities towards mineral dissolution rates. Three different cases were simulated: (1) flow through a 2D channel with a rough surface, (2) flow over rough single crystal surfaces, and (3) flow through an artificial rock (3D) model. All simulations were performed with COMSOL Multiphysics, using a finite element method (FEM).

2.1 Material

2.1.1 Surface topography analysis

In both 2D and 3D simulations, the fluid-mineral interface was defined using the rough surface topography of a calcite single crystal measured by interferometry microscopy, published in Bibi et al. (2018). There, the surface topography of a pre-reacted (10-14) calcite face with etch pits was measured over a dissolution period of 6 h. This resulted in the collection of 80 surface topography datasets by quasi-in situ measurements, allowing for the calculation of dissolution rates via difference maps. The topography selected for implementation in our RTM was measured towards the end of the dissolution experiment after 6 h (**Fig. 1 A**). This data set was selected because it exhibited the greatest variation in surface height, which is expected to have the strongest influence on hydrodynamics. The corresponding dissolution rate map was calculated using the height changes between 6 and 6.5 h. This rate map was then compared to rate maps simulated using different dissolution rate equations. The measured surface area was 414 µm x 313 µm with a maximum height variation of ~2.2 µm in the selected data set. A flow rate of 6 mL per minute was applied during dissolution, resulting in a residence time of < 8 s, ensuring conditions of surface-controlled reaction. Using the provided fluid volume of 0.5 mL and assuming a cubic shape, we can convert the flow rate to a flow velocity of ~1500 µm/s. In the 2D case, a single topography profile line was extracted parallel to the x-direction, resulting in a domain length of 414 µm (**Fig. 1 A,** blue line).

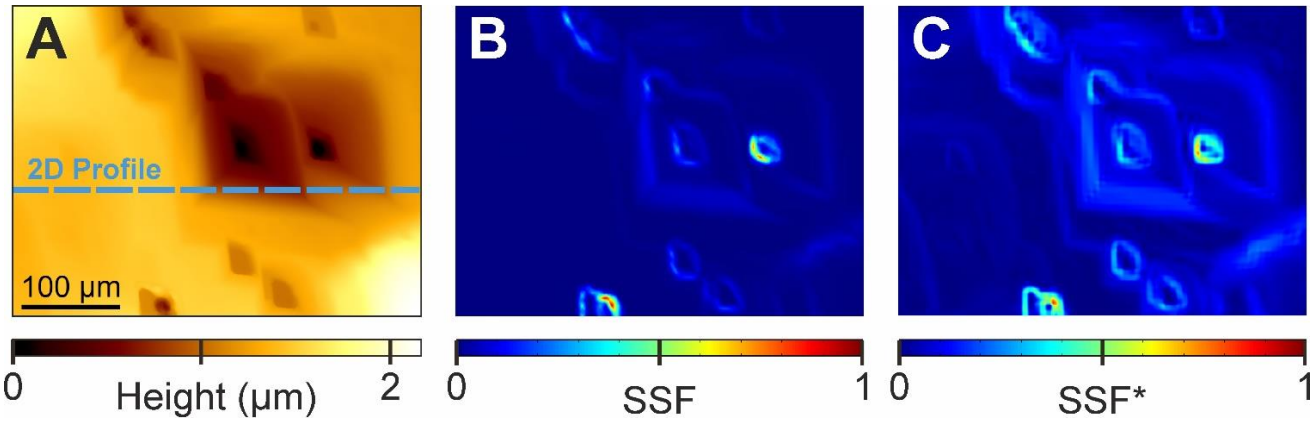

Figure 1: (A) Topography of the calcite single crystal surface selected for simulation. The topography is the same as the initial topography used for dissolution rate calculation in Fig. 4 h in Bibi et al. (2018). This surface map shows the largest height variation of all the initial topography measurements. The blue dashed line indicates the surface profile line used in the 2D simulations (cf. **Figs. 4** and **5**). (B) SSF distribution calculated using **Eq. (1),** based on the approach of Karimzadeh and Fischer (2021). (C) SSF* distribution with the improved slope equation (**Eq. (2)**). The improved equation shows much higher sensitivity, especially in the regions of low to intermediate slope (e.g. shallow etch pits) where the features could not be resolved previously.

2.1.2 Surface slope analysis and data treatment

Karimzadeh and Fischer (2021) suggested the use of surface slope as a way to parameterize the distribution of reactivity on mineral surfaces, which is not included in the classical rate equation approach. The concept is based on the heterogeneous distribution of reactive atomic sites on the surface as a function of local step density. This step density is higher in regions with strong height variations over small length scales compared to atomically flat planes (**Fig. 2**). At the µm scale, these height variations can be observed via the surface slope, with high slope values indicating a strong accumulation of atomic steps on the surface. Atomic steps consist of atomic surface sites with the highest reactivity for dissolution reactions: Step sites and in particular kink sites (Bollermann and Fischer, 2020). A high atomic step density may thus indicate a high concentration of reactive sites, leading to an overall increase in local reactivity. Areas of high surface tilt are mainly located at surface features such as etch pits and larger steps.

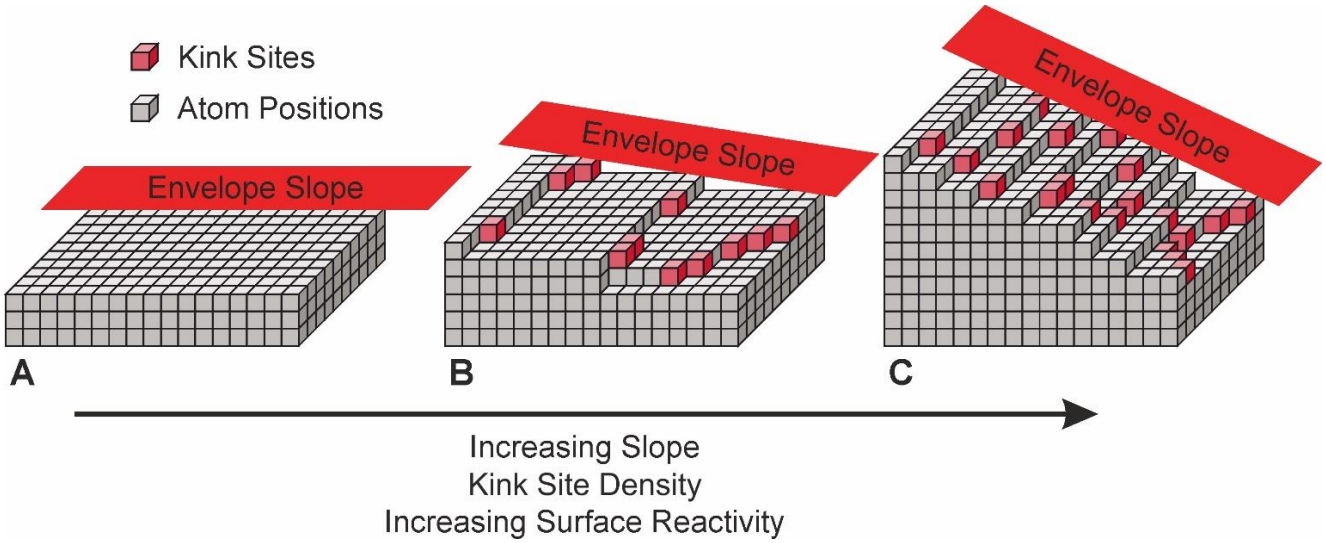

Figure 2: Schematic drawing of the surface slope on an atomic scale using the example of a Kossel-Stranski crystal surface. The envelope slope is represented by a red surface. (A) An atomically flat surface with no inclination and no crystal steps on the surface. (B) Crystal surface with a few steps leading to an intermediate slope. There are highly reactive kinks in the steps (red cubes). (C) Crystal surface with increased slope, resulting in higher step density and thus higher concentration of kink sites on the same surface. Based on this concept, the slope factor is used as a proxy parameter to describe the density distribution of steps and kinks and therefore the reactivity distribution on mineral surfaces.

Karimzadeh and Fischer (2021) calculated the SSF by using the surface gradient in the *z*-direction as a component of the surface normal vector perpendicular to the surface geometry:

$$SSF(x,y) = n_z = \nabla f(z) \tag{1}$$

This value can be calculated for any surface point, allowing the parameterization of each element at the interface. The resulting SSF distribution is shown in **Fig. 1 B**. The disadvantage of this calculation is that the general orientation of the surface must be perpendicular to the *z*-direction in order to capture a deviation using **Eq. (1)**. In real 3D systems with grains consisting of multiple surfaces, this approach is not applicable. To overcome this problem, we have improved the SSF equation to use the arctangent of the surface gradients of the normal vector in all spatial directions and relate it to the average orientation of the surface:

$$SSF^*(x,y) = \tan^{-1}(|nx - \overline{nx}| + |ny - \overline{ny}| + |nz - \overline{nz}|) \tag{2}$$

This allows SSF calculation independent of the spatial orientation of the surface. Additionally, this equation is more sensitive to low slope values. In comparison to **Fig. 1 B**, calculated **with Eq. (1)**, the new SSF* calculation increases the areas with low to medium SSF values and shows features such as shallow etch pits, which were not resolved by the previous calculation (**Fig. 1 C**).

2.1.3 Slope Factor Normalization

The relationship between dissolution rate and SSF must be adjusted by normalizing between the two values. Karimzadeh and Fischer (2021) and the present study use a simple linear SSF normalization. Here, the maximum rate corresponds to an SSF value of one, a rate of zero corresponds to an SSF of zero, and a linear distribution of rates mediates between the two extreme values. For our application to calcite single-crystal surfaces, this normalization produces results in good agreement with the experimental data, as presented in the following sections of this study. However, for different mineral systems, a more complex and case-adapted SSF normalization might be required. In general, there are two main options for adjusting the SSF normalization. The first is the slope of the normalization curve, which can be adjusted by changing the SSF value at which the maximum dissolution rate is reached. The gradient is used to describe the average kinetics of the complete crystal surface. As a second option, the shape of the normalization curve can be modified if a linear shape does not correctly represent the surface reactivity. Here, intermediate support points can be included in the SSF normalization to vary the gradient in specific regions where reactivity is increased or decreased in comparison to the average surface kinetics. Additionally, weighting factors can be included for local rate change in certain slope regions.

By using these control options, SSF can be applied to any crystal surface. Tuning of the SSF normalization needs to be performed by fitting simulation results to experimental rate spectra. Once a normalization with a good fit is achieved, it can be used for all further simulations with surfaces of the same mineral.

2.2 Fluid flow and transport

The simulation exemplifies the reaction kinetics in a single pore with a calcite crystal surface as pore wall in the micrometer range in a geological system (**Fig. 3**). Only slow fluid velocities were considered for fluid flow in the system (Reynolds number << 1). All simulations were performed at an average velocity of 1000 µm/s unless otherwise stated, similar to the estimated experimental velocity of 1500 µm/s. The fluid flow in our system was simulated assuming laminar flow conditions. The Navier-Stokes equation for the flow of an incompressible viscous fluid was applied:

$$\rho\left(\frac{\partial u}{\partial t} + u \cdot \nabla \mathrm{u}\right) = -\nabla p + \mu \nabla^2 u \tag{3}$$

$$\nabla \cdot u = 0 \tag{4}$$

where ρ is the fluid density (kg·m^{-3}), u is the fluid velocity (m·s^{-1}), t is the time (s), p is the fluid pressure (Pa) and μ is the dynamic viscosity (Pa·s). The flow was simulated above the calcite surface for a height of 75 µm in 2D, 30 µm in 3D, and 10 µm in 3D with moving boundaries. The geometry of the artificial rock is a cube with an edge length of 1500 µm. A fully developed flow or normal inflow velocity when using moving boundaries was applied at the inlet and a constant pressure condition was applied at the outlet. For the boundary interface with the calcite or other grain surfaces, the "no-slip" condition ($u = 0$) was applied. For the surface simulations, a leaking wall boundary condition with a fluid velocity in the x-direction was applied to the upper boundary, selected in proportion to the average flow velocity in the system ($u_{\mathrm{upper}} = 1.5 \cdot u_{\mathrm{avg}}$). For the two vertical boundaries parallel to the flow direction, the open boundary condition without viscous stress and without slip condition for moving boundaries was applied. For the artificial rock geometry, the calcite grain had the dimensions of 313 x 414 x 300 µm^3 and the additional inert grains had a radius of 400 µm for the large grain and 250 µm for the four small grains.

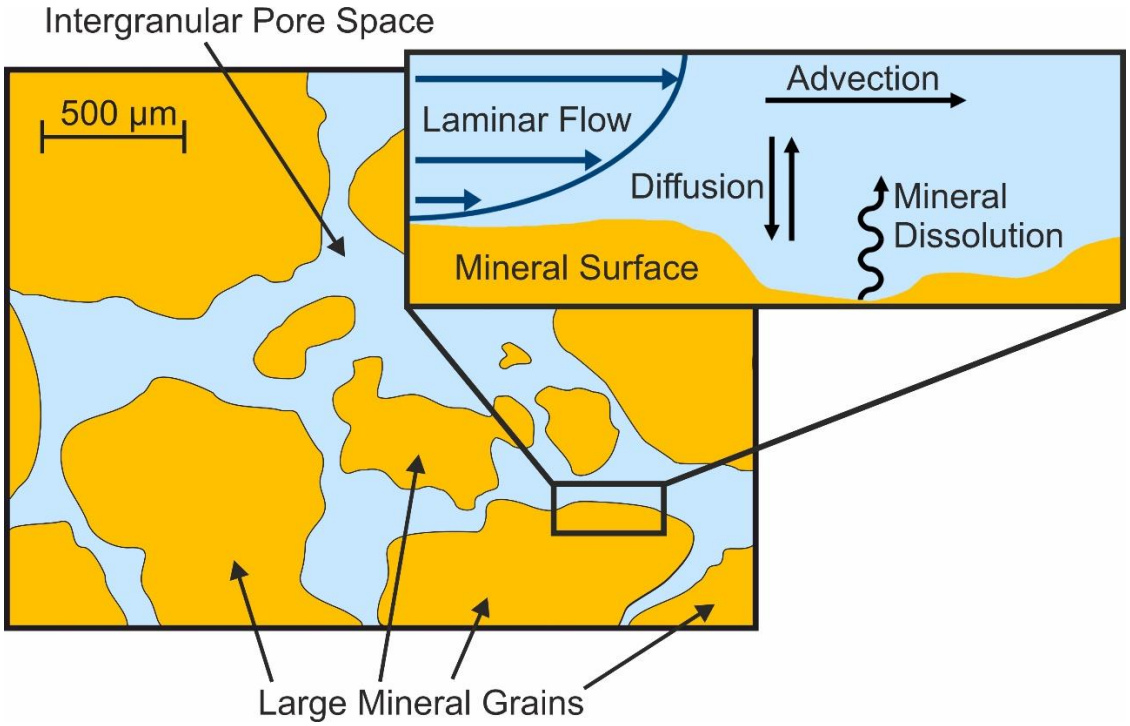

Figure 3: Schematic representation of a sedimentary rock consisting of larger grain components and intergranular pore space. The pore space can be filled with fine-grained minerals and cement or be empty and available for fluid flow. The inset shows an enlarged view of the mineral surface with all processes considered in the simulations.

For the simulation of species transport in the system, we applied the advection-diffusion-reaction equation for general transport:

$$\frac{\partial c_i}{\partial t} = \nabla \cdot (D_i \nabla c_i) - u \cdot \nabla c_i + R_i \quad (5)$$

where D_i is the diffusion coefficient ($m^2 \cdot s^{-1}$), c_i is the concentration ($mol \cdot m^{-3}$) and R_i is the reaction input ($mol \cdot m^{-3} \cdot s^{-1}$) of species i. Unless otherwise stated, a diffusion coefficient of $1 \cdot 10^{-9}$ $m^2 \cdot s^{-1}$ was used for all species in all simulations.

To quantify the importance of advection, diffusion, and reaction rates under different flow and transport conditions, two dimensionless parameters were used: The Péclet number (Pe) and Damköhler number (Da). The test of different flow conditions was performed in the 2D simulation case. The Péclet number is the ratio of the advection rate to the diffusion rate and is calculated as:

$$\mathrm{Pe} = \frac{u_{\mathrm{avg}} \cdot L}{D} \quad (6)$$

where L is the characteristic length (m). Here we selected the diameter of the flow channel for L. Pe > 1 shows an advection-dominated transport regime, whereas a Pe < 1 indicates a diffusion-dominated transport regime.

The Damköhler number relates the reaction time scale at the surface to the advection time scale and is calculated as:

$$\mathrm{Da} = \frac{T_{\mathrm{A}}}{T_{\mathrm{R}}} \quad (7)$$

$$T_{\mathrm{A}} = \frac{L}{u_{\mathrm{avg}}} \quad (8)$$

$$T_{\mathrm{R}} = \frac{C_{\mathrm{Calcite}}}{S_R} \quad (9)$$

where T_{A} is the advection and T_{R} the surface reaction time scale. C_{Calcite} is the density of surface sites of calcite ($mol \cdot m^{-2}$) and was obtained from Wolthers et al. (2008). S_R is the surface reaction rate ($mol \cdot m^{-2} \cdot s^{-1}$) and the reaction rate calculated at x = 100 µm was selected for the calculation of Da. Da > 1 indicates that the dissolution rate is limited by transport, while Da < 1 indicates dissolution rates limited by the surface reaction rate.

2.3 Geochemistry

As in the experiment, the solid phase in the model consisted of pure calcite. Initially, the species concentrations in the pore solution were adjusted to be in equilibrium with the calcite crystal surface, so that the dissolution was zero. At the beginning of the simulation, the concentrations in

315 the incoming fluid were slowly changed to obtain a solution with a pH of 8.82, as used in the
316 experiment of Bibi et al. (2018). All species concentrations of the initial equilibrium solution and
317 the influent solution are listed in **Table 1**. A zero gradient boundary condition was applied at the
318 outlet. All other boundaries except the fluid-mineral interface were modeled with a no-flux
319 boundary condition.
320

Table 1: Species concentration of the initial equilibrium fluid (Agrawal et al., 2020) and the influent fluid corresponding to the pH condition used in Bibi et al. (2018). CO_2 (gas) is removed from the system for the final 3D slope simulations to reduce the computational cost, while still adequately describing the system.

Species	**Equilibrium Solution (mol/m³)** (Agrawal et al., 2020)	**Inflowing Solution (mol/m³)**
CO_2 (gas)	$6.67 \cdot 10^{-4}$	31.622
CO_2 (aq)	$2.27 \cdot 10^{-5}$	$1.077 \cdot 10^{-2}$
CO_3^{2-}	$3.38 \cdot 10^{-2}$	$1.189 \cdot 10^{-1}$
HCO_3^-	$8.35 \cdot 10^{-2}$	$3.320 \cdot 10^{0}$
H^+	$1.27 \cdot 10^{-7}$	$1.589 \cdot 10^{-6}$
OH^-	$8.35 \cdot 10^{-2}$	$6.942 \cdot 10^{-3}$
Ca^{2+}	0.117	0
pH	9.91	8.82

321

322 At the interface, the surface of the calcite crystals can dissolve and release Ca^{2+} and CO_3^{2-} into
323 the solution. This was implemented by using a flux boundary condition. In RTMs, the dissolution
324 of the crystalline matter is usually simulated by applying a rate law according to transition state
325 theory (Lasaga and Lüttge, 2003; Steefel et al., 2015). For calcite, the standard rate law is:

$$Rate_{\mathrm{Calcite}}\left[\frac{\mathrm{mol}}{\mathrm{m}^2 \cdot \mathrm{s}}\right] = \left(k_1 \cdot a_{\mathrm{H}^+} + k_2 \cdot a_{\mathrm{CO_2(aq)}} + k_3 \cdot a_{\mathrm{H_2O}}\right) \cdot \left(1 - 10^{\frac{2}{3} \cdot \mathrm{SI}}\right) \tag{10}$$

$$\mathrm{SI} = \frac{a_{\mathrm{Ca^{2+}}} \cdot a_{\mathrm{CO_3^{2-}}}}{K_{\mathrm{sp}}} \tag{11}$$

326 where k_1, k_2 and k_3 are the reaction rate constants and a is the activity of all species involved in
327 the process. SI is the saturation index and is computed from the ratio of the ion activity product
328 and the solubility constant K_{sp}. There are multiple sources from literature for the reaction rate
329 constants and the solubility constant (Busenberg et al., 1986; Plummer et al., 1978). In our model,

we use the values reported by Chou et al. (1989): k_1 = 8.9·10^{-5}, k_2 = 5.0·10^{-8}, k_3 = 6.5·10^{-11} and K_{sp} = 10$^{-8.46}$ at 25°C.

To describe surface reactivity in the rate equation, we include the previously introduced SSF as a simple factor dependent on the local slope values:

$$Rate_{SSF}(x,y) = SSF(x,y) \cdot Rate_{\mathrm{Calcite}}(x,y) \tag{12}$$

2.4 Simulation of Topography Evolution

In order to simulate the changing topography of the crystal surface with proceeding dissolution, we introduced a moving boundary condition for the calcite surface and the calcite grain. We used the "deformed geometry" function available in COMSOL for this calculation. Based on the local dissolution rate, we calculated a local surface retreat velocity v (m·s^{-1}) using the molar volume of calcite $\mathrm{V_m}$ (m^3·mol^{-1}):

$$\mathrm{v_{Retreat}(x,y)} = \mathrm{Rate_{\alpha}(x,y)} \cdot \mathrm{V_m} \tag{13}$$

This retreat velocity was then applied to the dissolving calcite surface, which in turn can change the slope and therefore the reactivity distribution as the simulation time progresses. Over larger simulation times, height changes of up to several micrometers can be simulated.

3. Results and Discussion

The results of this study are presented in five sections, each consisting of results section followed by a discussion section. In the first section (3.1), we use a 2D cross-sectional simulation over the rough calcite surface to evaluate the influence of hydrodynamics on the surface dissolution rate. In a second step (3.2), we compare the classically simulated dissolution rates with experimental data and focus on specific crystal surface sections to investigate whether the classical approach can adequately describe the mineral dissolution. In subchapter 3.3, simulation results using the new SSF parameterization are compared to both, the classical simulation approach and experimental results. Subsection 3.4 examines the temporal evolution of the surface topography and the prediction of the dissolution rate using the new SSF parametrization and including the spatial modification of surface reactivity. In the final step (3.5), the reactivity parameterization is applied to an artificial 3D rock geometry, in contrast to the simpler situation of a single crystal surface. Here we compare results to calculations without reactivity parameterization and highlight the differences. We show a pathway to apply the surface-dependent SSF for use with realistic rock geometry data.

3.1 Influence of heterogeneity of surface topography on transport and reaction rates (2D simulation)

3.1.1 Results

In this RTM, we simulated dissolution rates along the calcite-fluid interface with rough topography available from VSI data. We varied the reaction and transport conditions at the surface by changing flow velocities and diffusion coefficients. The flow velocities were used to control surface dissolution rate limitations (Da), with low flow velocities leading to transport-controlled conditions and high flow velocities leading to surface reaction rate-controlled conditions. The main transport mode, advection or diffusion, was controlled by varying the diffusion coefficients. All selected flow velocities and diffusion coefficients, as well as the resulting Pe and Da numbers for the eight simulated cases, are presented in **Fig. 4**. The resulting calcium concentration profiles up to 2 µm above the calcite surface are shown in **Fig. 4**. Calcium is released only by the dissolution reaction at the surface, as the inflowing fluid has a calcium concentration of zero.

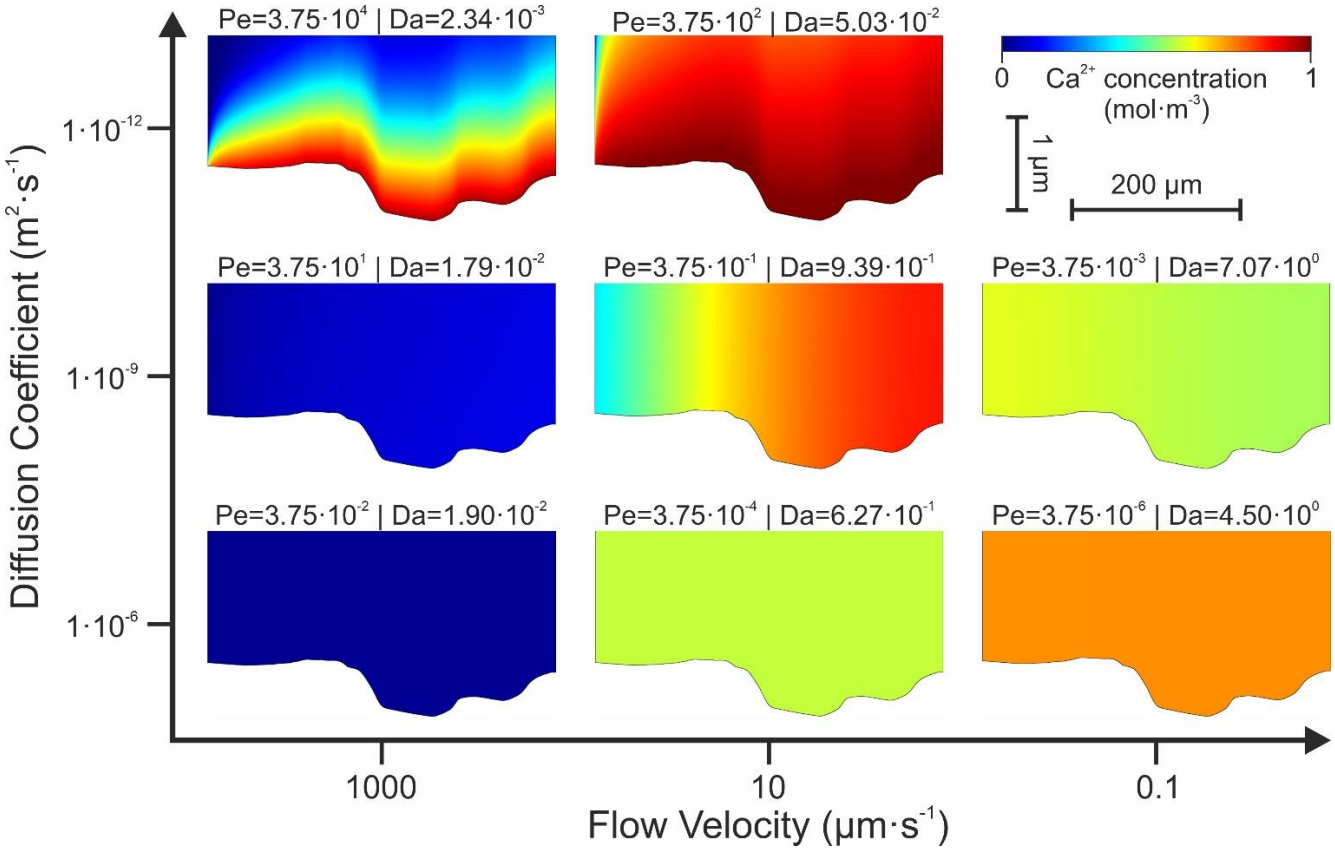

Figure 4: Simulated Ca^{2+} concentration profiles up to 2 µm above the rough calcite surface under different transport and reaction conditions. The respective Péclet and Damköhler numbers are given for each case. Advection-controlled (Pe > 1) conditions lead to boundary layer formation with high concentration of solute species. Diffusion-controlled conditions (Pe < 1) result in a homogeneous distribution of solute species. Higher flow velocities result in overall lower Ca^{2+} concentrations in the domain. Experimental conditions ($u \approx 1500$ µm/s, $D \approx 1 \cdot 10^{-9}$ $m^2 \cdot s^{-1}$) in Bibi et al. (2018) are expected to lead to a solute concentration distribution similar to the case with high flow velocities and intermediate diffusion coefficient (Pe = $3.75 \cdot 10^1$, Da = $1.79 \cdot 10^{-2}$).

When diffusive transport dominates in the system (cf. cases in the bottom row), the calcium released from the surface is homogeneously distributed in the liquid without any gradient being observed. An increasing in fluid velocities under diffusion-dominated conditions causes an overall lower calcium concentration in the fluid (cf. case at bottom right vs. case at bottom left). Under transport conditions where the influence of advective transport increases, a concentration gradient is developed from the inlet to the outlet (cf. case in the central section). This effect is better observed in the simulations with low diffusion strength (cf. case in the upper left). Predominant advective transport leads to the formation of a boundary layer with high calcium concentration and to the formation of a concentration gradient between the surface and the center of the flow channel (cf. case in the upper left). The thickness of the boundary layer decreases with increasing velocity. We expect that the experiment in Bibi et al. (2018), based on the estimated experimental

conditions of $u \approx 1500$ µm/s and $D \approx 1 \cdot 10^{-9}$ $m^2 \cdot s^{-1}$, leads to a concentration distribution similar to the case with high flow velocity and intermediate diffusion (Pe = $3.75 \cdot 10^{1}$, Da = $1.79 \cdot 10^{-2}$).

For all simulation cases, the dissolution rates based on the classical rate equation along the interface from inlet (x = 0 µm) to outlet (x = 414 µm) are shown in **Fig. 5**. When diffusion is the dominant transport mode, the dissolution rates are constant over the entire length. A decrease in fluid flow rate under these conditions is expected to change the limitation of the reaction rate from surface- to transport-controlled conditions. The only visible effect in the simulation results is the decrease in the overall dissolution rate while it remains constant along the interface. With increasing advective transport, a gradient in dissolution rate is observed from the inlet to the outlet. At the highest advective influence, a high gradient near the inlet is followed by a low dissolution rate, which is largely constant. As expected, dissolution rates increase with flow velocity and surface reactivity control until a near-zero calcium concentration is reached in the fluid, where the rate maximum is observed. This result is similar to the dissolution plateau reported by Liang and Baer (1997), which occurs when dissolution is controlled solely by the surface reaction rate.

The comparison between RTM and experimental reveals a large difference in the behavior of the dissolution rate. The experimental rate shows a constant baseline dissolution with distinct peaks at certain locations on the surface. These locations are the steps forming the two etch pits included in the selected profile line. In none of the simulated cases are there peaks in the dissolution rate that could be associated with features of the surface topography such as steps. Comparison of the experimental results with the simulation case with similar conditions (Pe = $3.75 \cdot 10^{1}$, Da = $1.79 \cdot 10^{-2}$) reveals two major differences. First, the overall rate is overestimated in the model with an average rate of about $4 \cdot 10^{-6}$ $mol \cdot m^{-2} \cdot s^{-1}$, whereas in the experiment a maximum rate of about $1 \cdot 10^{-6}$ $mol \cdot m^{-2} \cdot s^{-1}$ is reached when it peaks. Second, no rate peaks are observed in the RTM, and a gradient is predicted that is not seen in the experimental data. Even with a wide range of conditions, the RTM is not able to reproduce the experimental result.

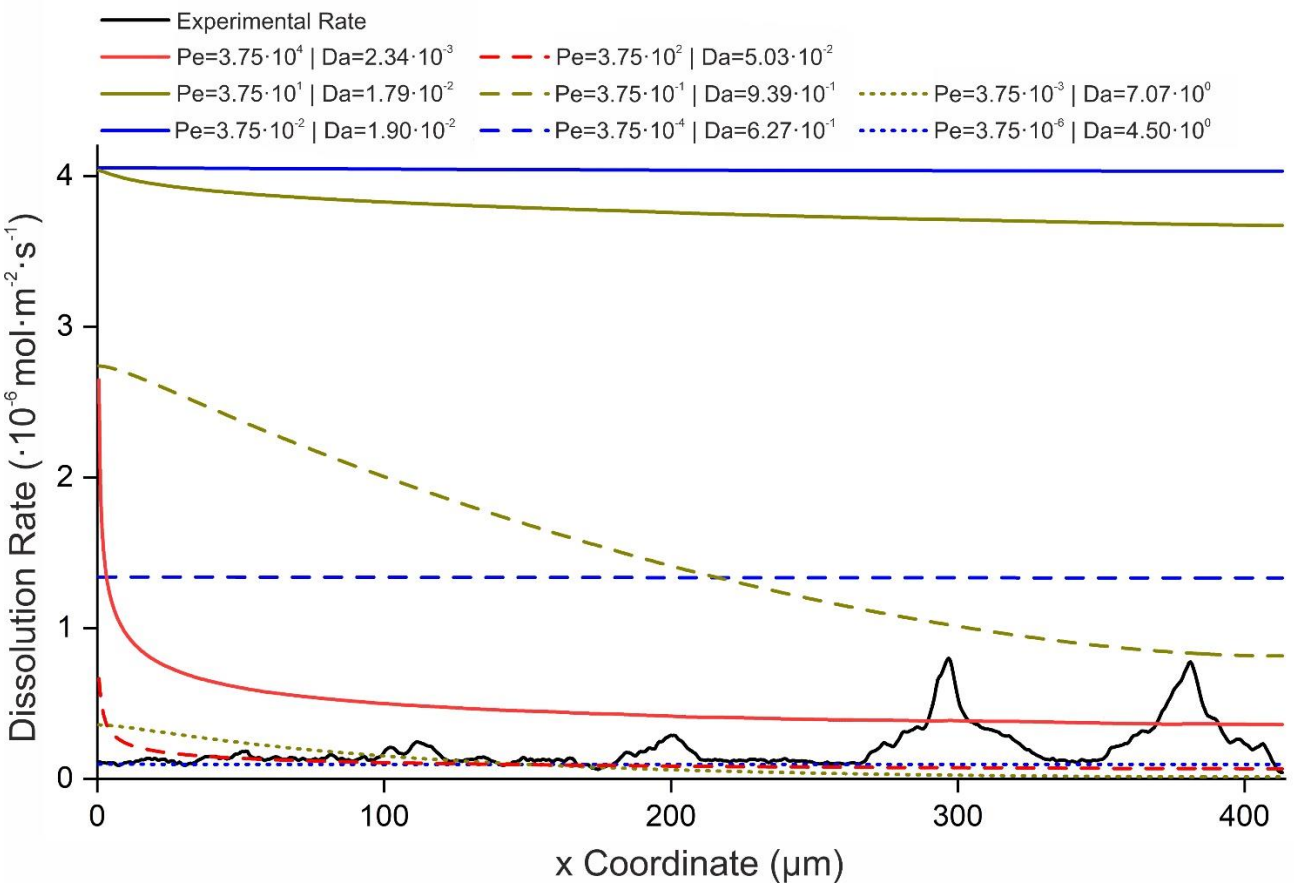

Figure 5: Calcite dissolution rate at the topographic boundary under different flow and transport conditions: Blue for high *D*, yellow for intermediate *D*, and red for low *D* values. Solid lines represent high *u*, dashed lines intermediate *u,* and dotted lines low *u* values. The arrangement of the color scale legend corresponds to the image setup in **Fig. 4**. Strong diffusive transport leads to a constant dissolution rate. With decreasing influence of diffusive transport, the rate follows a decreasing gradient from inlet to outlet. Higher flow velocities increase the overall dissolution rate. No rate variability is visible under any condition, in contrast to the rate variability in the experimental profile. Experimental conditions were set to satisfy Pe > 1, Da < 1 (Bibi et al., 2018; Liang and Baer, 1997).

3.1.2 Discussion

Hydrodynamic conditions can play a key role in the distribution of dissolution rates on mineral surfaces. Under transport-controlled conditions, the flow velocity and diffusion of solute species are the key parameters describing the dissolution reactions and thus determine their distribution. When shifting to a surface reactivity-driven dissolution regime with high transport efficiency due to high flow velocities or diffusion, the mineral surfaces exhibit a heterogeneous distribution of rates, as shown by measurements using surface-sensitive techniques (Bibi et al., 2018; Fischer et al., 2014). Do hydrodynamic effects cause and/or modify this heterogeneous rate pattern or is it dictated solely by intrinsic crystal properties (Agrawal et al., 2021; Fischer et al., 2014)?

To answer this question, we investigate the species concentrations at different transport conditions during the dissolution reaction. The simulations with conditions matching the experimental

specifications failed to reproduce the heterogeneous distribution of the dissolution rate. The topography of the mineral surface can affect the fluid flow and create concentration gradients leading to varying dissolution rates. A similar effect has been reported by Deng et al. (2018), who used RTM to study pore-scale dissolution of calcite at rough pore walls. They reported that an increase in surface roughness due to a larger surface area resulted in an overall increase in the dissolution rate. This increase is not linear, as increasing roughness creates immobile or recirculating fluid zones in surface pits. Here, the concentrations of dissolved ions increase, limiting the dissolution rate via a high local saturation (**Eqs. 11** and **12**). However, the surface roughness applied by Deng et al. (2018) produces pits with a wide range of depth-to-width ratios (d/w ratio), ranging from 1 : 5 to 1 : 20. In contrast, the d/w ratios observed on the reacted crystal surface show values 1 : >85. No formation of recirculation zones was observed in our simulations. The only rate-decreasing effect under the experimental conditions is some hydrodynamic shadow regions, which are responsible for only a very small rate reduction. Calculations show that such rate decrease is about two to three orders of magnitude below the overall dissolution rate for d/w ratios of 1 : >85. This rate decrease is less than the line width of the VSI rate curve in **Fig. 5**. In comparison, for an artificial cuboidal pit on a flat surface, the concentration accumulation in a pit with a depth-to-width ratio of 1 : 100 results in a 0.1% rate decrease, while a pit with a ratio of 1 : 10 results in a 1% decrease. Rasoulzadeh et al. (2020) report similar results where they investigated the influence of sinusoidal pits (~1 : 2 d/w ratio) on calcite dissolution rates. The difference in dissolution rates between sine maximum and minimum is << 1%, and at higher Reynolds numbers the rate maximum shifts towards the wall facing the fluid flow. Other numerical studies have shown similar results in the past. Harb and Alkire (1989) investigated the growth of corrosion pits using a finite element model. Their simulations of a shallow, rounded pit (d/w ratio ~ 1 : 3.5) on the pore wall show that flow can enter the pit without forming recirculation zones whose flow velocity decreases only slightly. The simulated concentration of dissolved ions showed an increased concentration in the center of the pit. In the simulations of fluid flow over circular pits by Higdon (1985), the importance of pit width relative to depth for the formation of recirculation zones can be observed. In the case of the shallowest simulated pit (d/w ratio ~1 : 4.5), the flow field can enter completely into the center of the pit. As the pit depth increases (up to a d/w ratio ~ 1 : 2), a recirculation zone forms at the bottom of the pit, similar to the results of Deng et al. (2018).

The reported rate reduction effect is strongest in the surface pits. In contrast, the experimental data show that the highest reaction rates are found at the positions of the two largest etch pits on the profile (**Fig. 5**). Thus, we conclude that there appears to be a competing effect between the rate reduction due to local hydrodynamics and the rate increase due to the high local surface

458 reactivity at the etch pit walls. Therefore, neglecting surface reactivity in RTMs leads to an
459 incomplete description of the dissolution. Agrawal et al. (2021) investigated calcite surface
460 sections of smaller dimensions (21 µm) that exhibited pits with higher d/w ratios (1 : 2.5) in an
461 RTM due to the polycrystalline nature of the sample. Their results confirmed the absence of
462 transport-controlled rate variability in the experimental approach. Overall, these studies confirmed
463 the general conclusion about intrinsic dissolution rate variability. Nevertheless, the elevated and
464 constant rates of the simulation results (**Figs. 5** and **6**) require a new numerical treatment
465 (Karimzadeh and Fischer, 2021).

3.2 Mineral dissolution under surface controlled conditions (3D simulation)

3.2.1 Results

The dataset investigated by Bibi et al. (2018) covers a relatively large field of view (FOV) compared to the FOV investigated in previous studies, e.g., Agrawal et al. (2021) with surfaces of 21 x 21 μm^2 and Karimzadeh and Fischer (2021) with 95 x 95 μm^2. Additionally, a long reaction period of 6 h is covered by around 80 individual surface measurements in the present dataset. Thus, this dataset provides several important clues for the validation of an RTM parametrization focusing on the reactivity of the crystal surface.

To cover specific parts of the surface reactivity, the 3D calcite surface is divided into three separate cases for simulation, shown in **Fig. 6**. Case (A) consists of the complete measured surface from Bibi et al. (2018) (**Fig. 1** A) with a FOV of 414 × 313 μm^2. Two subsections are selected to cover the extreme features of the surface topography: the deepest etch pit on the surface (B) with a FOV of 116 × 105 μm^2 and the highest step structure (C) with a FOV of 101 × 100 μm^2. All simulations here use the same flow velocity (1000 $\mu m \cdot s^{-1}$) and diffusion coefficient ($1 \cdot 10^{-9}$ $m^2 \cdot s^{-1}$), identical to the 2D simulation with Pe = $3.75 \cdot 10^{1}$ and Da = $1.79 \cdot 10^{-2}$, which we expect based on the experimental constraints (**Figs. 4** and **5**). **Figure 6** shows the surface topography (I) and the experimental dissolution rate (II) and compares them with the model result (III and IV). Row V shows the difference in dissolution rates between a model with the VSI surface topography and a model with a flat surface of the same size to quantify the influence of surface topography. The maps of experimental dissolution rates show the heterogeneous distribution of dissolution rates discussed previously, which can be associated with the surface topography structures such as etch pits and steps. In contrast, the simulation yields a very similar rate distribution for all three cases. Two effects are observed when comparing the models with the VSI surface to a model with a flat surface (**Fig. 6** V). The first effect consists of numerical errors visible for the smaller model sizes of cases (B) and (C), caused by random local minima or maxima in the hydrogen concentration along the lateral boundaries. This could be due to chosen boundary conditions. The second effect shows a decrease in the dissolution rate at the locations of the etch pits, similar to the effect discussed in Section 3.1.2. In our simulation, this decrease in dissolution rate caused by transport is two to three orders of magnitude smaller than the calculated rate and therefore does not significantly affect the overall rate distribution. For the large surface step, no visible effect of topography on the dissolution rate can be detected.

Further details on the dissolution rate distribution can be derived from the rate spectra of the respective cases for RTM and experiment (**Fig. 7**). The rate spectrum for the entire surface shows

a single peak at around 0.2 $\cdot 10^{-6}$ mol$\cdot$m$^{-2}\cdot$s^{-1} and a large range of dissolution rates >2 $\cdot 10^{-6}$ mol$\cdot$m$^{-2}\cdot$s^{-1}. The two subsections show different contributions. At the large etch pits, the overall reactivity is increased compared to the entire surface, but the general distribution of the spectrum remains similar. No clear peak is visible at the surface step, but a wide range of surface portions with higher rate contributions is seen. In contrast, the RTM rate spectra show a completely different rate distribution. All rates are >3.6 $\cdot 10^{-6}$ mol$\cdot$m$^{-2}\cdot$s^{-1} and the maximum range of rates is <0.4 $\cdot 10^{-6}$ mol$\cdot$m$^{-2}\cdot$s^{-1} for the entire surface, resulting in an almost singular rate value. The smaller surface sections show the same rate distribution, but with a shift of the minimum value to higher rates. This shift is due to the small rate gradient from inlet to outlet mentioned earlier, which decreases as the surface sections become smaller. Here, the rate is even more confined to a small range. The rate spectra confirm the large discrepancies between model and experiment observed in the rate maps.

In general, the RTM dissolution rate distribution closely resembles the previous 2D result and does not reproduce the experimental findings with the same sample topography. Only a minor influence of topography was observed, which does not contribute significantly to the overall rate distribution.

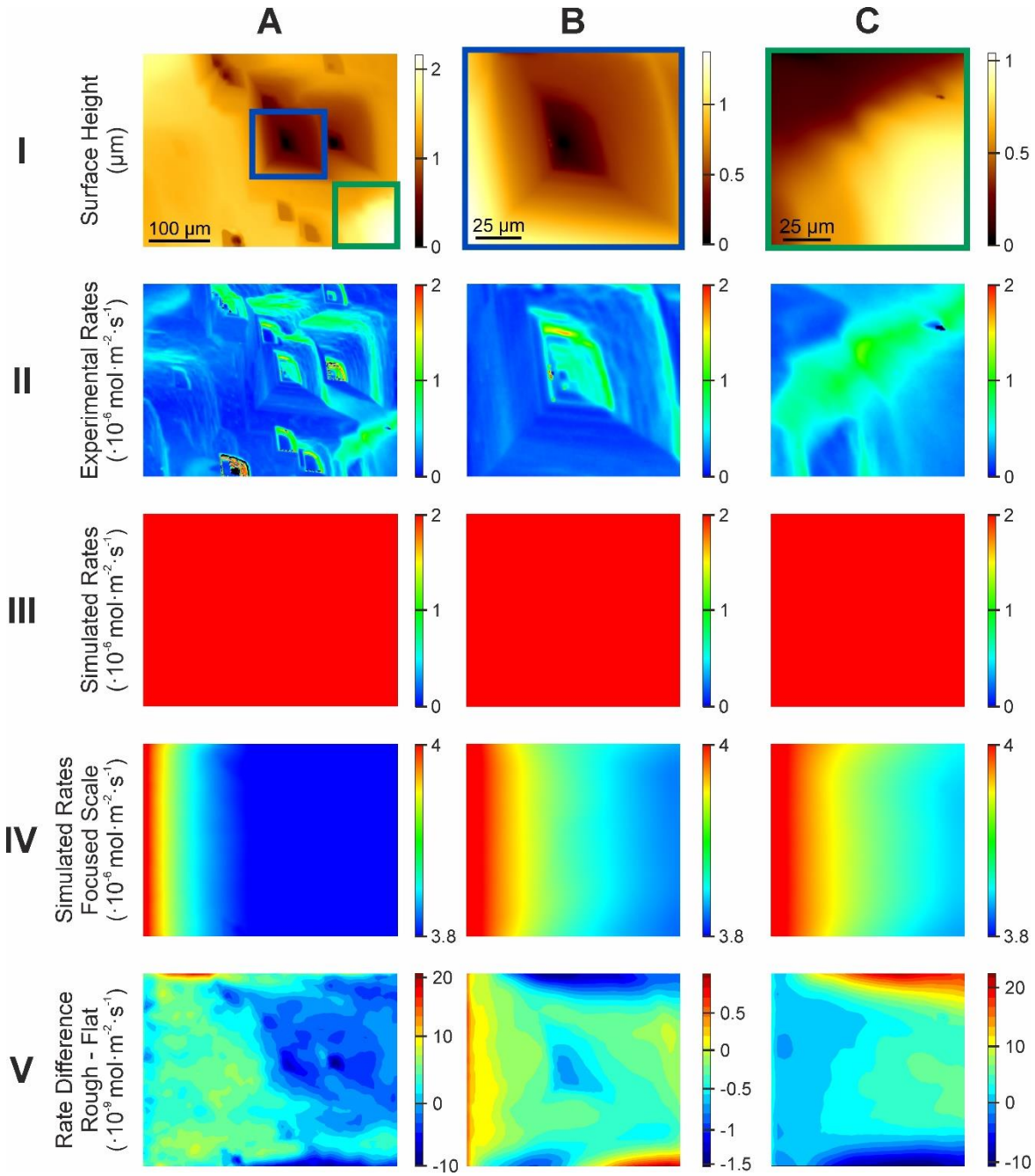

Figure 6: (A) Full data set of calcite single crystal surface with the two areas of interest for detailed investigation marked on the height map: (B) large etch pit and (C) large surface step. For all areas, (I) the height, (II) the experimental dissolution rate, (III) the simulated rate, and (IV) the difference in dissolution rate between the rough and flat mineral surface are shown. From the comparison of the maps of experimental (II) and simulated (III) dissolution rate, a clear difference is observed. The effect of topography on the simulated rates is two to three orders of magnitude less than the rate itself (IV). Pit locations show a decreased dissolution rate in the RTM (A-IV, B-IV), while the large step shows no effect on the dissolution rate (C IV). Numerical boundary errors are observed along the lateral boundaries in the difference maps (IV). These errors have only a minor influence on the total simulated dissolution rate (III).

517

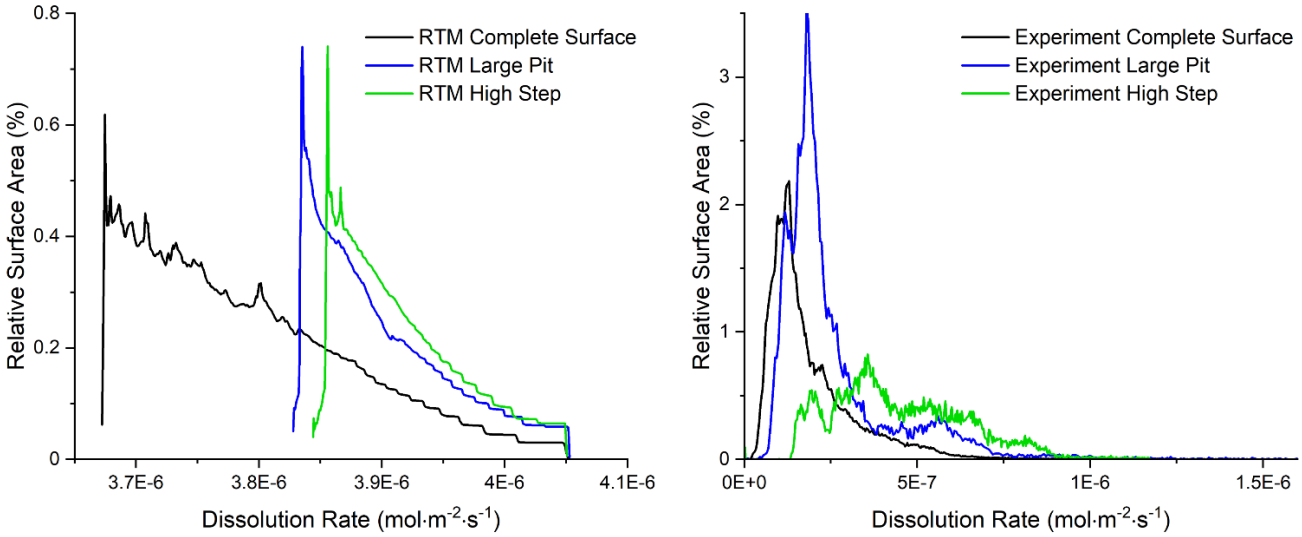

Figure 7: Rate spectra corresponding to the rate maps shown in **Fig. 6** for the simulated (left) and experimental (right) results. The spectra highlight the strong differences in dissolution rates between RTM and experiment. The RTM predicts rates that are four times higher than the observed rates. The range of simulated rates is much narrower and is close to a single value for the entire surface.

3.2.2 Discussion

In agreement with the results from 2D RTM, the 3D simulations are not able to reproduce the experimental dissolution rate maps measured by Bibi et al. (2018). The reason for this discrepancy is the lack of a description of surface reactivity in the widely used calcite rate equation (**Eq. 10**). In both our simulations and the experimental setup used to measure surface dissolution rates, hydrodynamic conditions lead to a surface-controlled dissolution rate regime. Above a threshold, a further increase in flow rate does not lead to any additional increase in dissolution rates (Liang and Baer, 1997). Here, the influence of transport on rates is negligible. Mineral intrinsic effects are thus the cause of the observed variabilities in dissolution rates under such conditions.

Various experimental studies have confirmed a heterogeneous distribution of dissolution rates under the same transport conditions (Arvidson et al., 2003; Bollermann and Fischer, 2020). A large difference was found between the dissolution rates of powders and mineral surfaces, which was explained by the different concentration of reactive sites (Arvidson et al., 2003). This highlights the limited applicability of single rate constants derived from powder measurements such as Busenberg et al. (1986) for the calculation of dissolution rates under surface-controlled reaction conditions. On mineral surfaces, larger structures such as etch pits or macrosteps show greater intrinsic reactivity than flat surface sections (Pollet-Villard et al., 2016). These structures evolve over time through step motion, leading to the widening of etch pits, the formation of larger

steps, and the generation of new stepwaves (Bibi et al., 2018; Fischer and Luttge, 2018). It has been shown that the use of the stepwave model in an RTM improves the description of calcite dissolution (Bouissonnié et al., 2018). Bollermann and Fischer (2020) have highlighted the importance of multiple rate components that rely on surface building blocks to cause the formation of various topographic features. A comprehensive review of surface reactivity can be found in Fischer et al. (2014). The lack of an implementation of surface reactivity in the RTM rate equation leads to the results presented (**Fig. 6** and **7**), which incorrectly predict the rate distribution and magnitude in our system.

Atomic-scale modeling provided additional mechanistic insight into the influence of reactive atomic sites and their distribution on mineral surfaces on dissolution rates and was able to confirm previous experimental findings (Kurganskaya et al., 2012; Lasaga and Lüttge, 2003). Numerical approaches that do not include the mineral surface reactivity in their rate description are not able to achieve the same results (Agrawal et al., 2021). The effect of natural calcite surface topography on fluid flow and hence transport is small ($< 2 \cdot 10^{-8}$ mol·m^{-2}·s^{-1}) compared to the total simulated ($\sim 4 \cdot 10^{-6}$ mol·m^{-2}·s^{-1}) or experimental ($> 2 \cdot 10^{-6}$ mol·m^{-2}·s^{-1}) dissolution rates.
The recent publications by Agrawal et al. (2021) and Karimzadeh and Fischer (2021) confirm this small effect of natural mineral surfaces on the transport efficiency in the system and thus on the dissolution rate. In conclusion, the results of classical 3D RTM highlight the need for parameterization of reactivity in dissolution rate calculations, recently reported by Agrawal et al. (2021) and Karimzadeh and Fischer (2021).

3.3 Newly-parameterized 3D RTM towards surface rate variability

3.3.1 Results

Based on the slope parameterization (SSF) approach recently developed by Karimzadeh and Fischer (2021), an improved SSF* calculation was developed (**Eq. 2**). This new parameter improves the sensitivity to shallower surface structures and can be applied independently of the surface orientation in the model. In the parameterized RTM, the SSF* is calculated for all elements of the mesh on the calcite surface (**Fig. 1**) and used as a factor in the classical rate equation (**Eq. 12**). The distribution of the linear SSF* normalization for the calcite surface is shown in **Fig. 1 C**. The simulation uses the same flow and transport conditions as the previous 3D simulations (u = 1000 µm·s-1, $D = 1 \cdot 10^{-9}$ $m^2 \cdot s^{-1}$).

The application of SSF* strongly alters the RTM simulation results in terms of dissolution rate (**Fig. 8**). The resulting dissolution rate map shows a largely heterogeneous distribution of rates, very similar to the distribution in the experimental counterpart (**Fig. 6 A II**). High dissolution rates are concentrated in the deep etch pits and large steps of the calcite surface. Intermediate rates are found at shallower etch pits and smaller steps on mostly flat surface areas. Surface areas without any structures show dissolution rates close to zero, similar to the experimental results. Overall, we conclude that the simulation results are in good agreement with the measured data with respect to the heterogeneous rate distribution. This conclusion is supported by the comparison between the rate spectra of the parameterized RTM and the experiment. Both datasets show a single high rate peak, which is $1.3 \cdot 10^{-7}$ $mol \cdot m^{-2} \cdot s^{-1}$ in the experiment and at $0.6 \cdot 10^{-7}$ $mol \cdot m^{-2} \cdot s^{-1}$ in the simulation. At higher dissolution rates, the percentage of the surface decreases to values close to zero, with only small sections contributing the highest dissolution rates. The overall range of dissolution rates is in much better agreement with experimental observations compared to the previous model (0 to $2 \cdot 10^{-6}$ $mol \cdot m^{-2} \cdot s^{-1}$). The previously observed rate gradient between inlet and outlet can no longer be observed, as it has little effect on the total dissolution rate ($< 0.4 \cdot 10^{-6}$ $mol \cdot m^{-2} \cdot s^{-1}$). Application of the previously developed SSF (Karimzadeh and Fischer, 2021) leads to a divergent map of the dissolution rate, similar to the SSF distribution in **Fig. 1 B**. In the rate spectrum, the SSF parameterization yields 40 % of the surface with zero dissolution rate. These differences highlight the improved sensitivity of the new SSF* calculation towards smaller rate contributions to the dissolution rate spectrum. The implementation of the SSF* leads to improved overall agreement between the dissolution rates in the experiment and the RTM in compared to the classical RTM and the previous SSF approach. As a first-order parametrization, the surface slope can adequately describe the surface reactivity distribution associated with the surface topography.

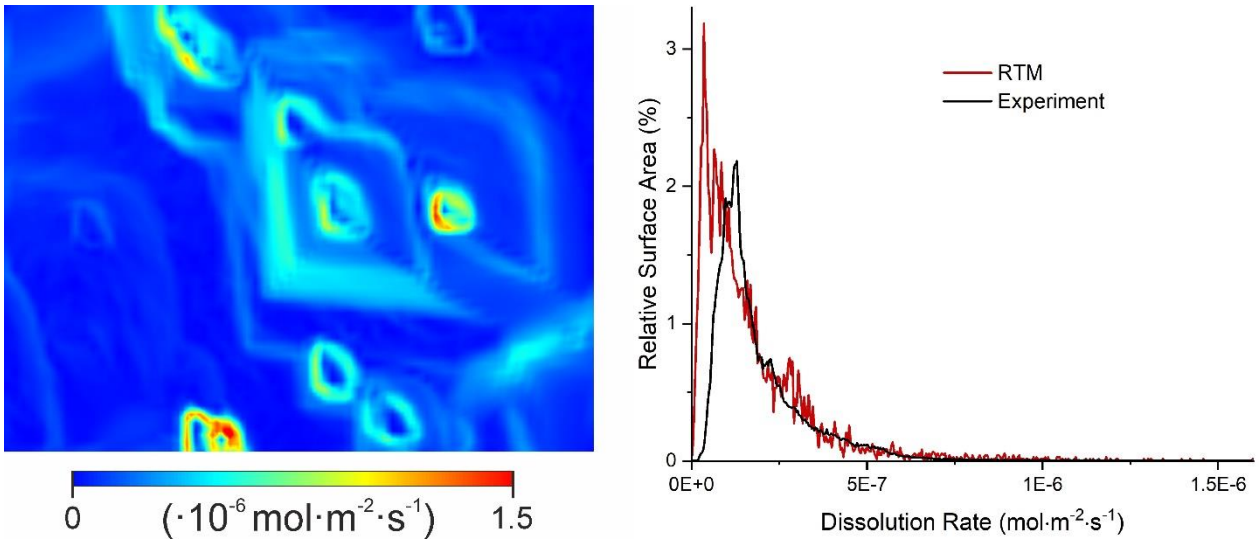

Figure 8: Left: Dissolution rate maps created with the improved slope factor parameterization using the surface topography from **Fig. 6** A I. The implementation of the slope factor enhances the influence of surface steps and pits on the dissolution rate, as can be observed in the experimental rate map (**Fig. 6** A II). Compared to the previous RTM results (**Fig. 6** A III), the agreement between simulation and experiment is greatly improved. Right: Comparison of the dissolution rate spectra between the improved RTM approach with slope factor and the experimental results shows the better agreement compared to the previous RTM approach (**Fig. 7**).

3.3.2 Discussion

The inclusion of surface reactivity in the dissolution rate equation via the surface slope leads to results that agree well with experimental measurements. This confirms the results of Karimzadeh and Fischer (2021), who first introduced the use of surface slope as a proxy for reactivity. The involvement of surface normal components in the improved SSF* resulted in a remarkable improvement regarding the sensitivity of the parameterization to small rate contributions at the surface. With the previous SSF, nearly half of our sample surface would exhibit zero dissolution rates, showing large differences from experimental observations. Additionally, the new equation allows for spatially independent calculation of surface reactivity, which is required for 3D datasets with whole crystal grains. The major advantage of reactivity parameterization via slope is that no prior knowledge of the surface reactivity distribution is required once a good normalization is established. Agrawal et al. (2021) included reactivity in their model by using the dissolution rate map available from experimental measurements. This approach is not practical for crystal surfaces without prior experimental dissolution data and cannot predict the evolution of reactivity as reaction time progresses. The SSF* parameterization presented can be applied to any new calcite surface and approximate its reactivity on a first-order basis.

The theoretical basis of the SSF* is obviously correct, since it can reproduce the reactivity distribution. A high slope value may indicate a high concentration of atomic-scale steps on the surface. These steps consist of multiple differently coordinated atomic sites (Luttge et al., 2013). Most important for the dissolution reaction is the high concentration of kink sites located at the atomic steps on the surface (Fischer et al., 2014). Kinks are comparatively easy to dissolve from the surface and can propagate on surface features such as steps. Thus, for calcite, the distribution of kink sites primarily controls the overall dissolution rate (Kurganskaya and Luttge, 2016). To predict surface reactivity, one must be able to predict the distribution of kink sites. At the pore-scale, the slope of a mineral surface can describe the distribution of kink sites as a first-order approximation.

A potential issue in parameterizing the slope is known as step bunching. In this process, atomic steps can catch up with the preceding step and form stable steps of larger vertical heights (Amelinckx et al., 1957; Schwoebel and Shipsey, 1966). Bunched steps dissolve more slowly than single atomic layer steps as they lose kink sites during bundling of multiple single layer steps (Cheng and Coller, 1987). Bunching cannot be resolved with the slope value because one large step can give the same value as several small steps. This might lead to an incorrect prediction of surface reactivity by the SSF* calculation.

The key to a precise approximation of reactivity is the normalization of the SSF*. As already described in the methods section, we use a simple linear normalization where a SSF* value of one is equal to the maximum simulation rate. For the calcite surface, this normalization leads to a good approximation of the experimental data. However, such normalization is most likely not universally applicable to other crystal surfaces. It is also possible that differently oriented surfaces on the same crystal require separate normalizations of the slope factor, as observed in experiments (Saldi et al., 2017). In a more complex normalization, the overall slope of the normalization curve can be changed to tune the overall surface reactivity. If certain rate regions are over- or underestimated, sections of slope values in the rate can be decreased or increased to match the experimental rate spectrum across defined support points.

In conclusion, our results confirm that slope parameterization can provide a good approximation of first-order surface reactivity. This improvement in the reactivity description for RTMs is essential for simulating the system under surface-controlled conditions, especially in natural environments at the pore scale.

3.4 Temporal evolution of dissolution rates

3.4.1 Results

A moving boundary based on the surface retreat velocity (**Eq. 13**) was implemented to observe surface topography evolution due to material flux over longer dissolution periods, and its influence on the simulated rate. The surface retreat is simulated for 6 h and the SSF* is renormalized at each intermediate time step.

Initially, strong surface retreat occurs at the etch pit walls due to the high concentration of high dissolution rates there (**Fig. 9**). As dissolution progresses, a widening of the etch pits is observed, with the etch pit walls moving outward from the central pit axis. The shift of the etch pit walls results in accompanying movement of regions of high reactivity due to the high slopes. This movement follows the crystallographically controlled shape of the calcite etch pits and is best seen in the two largest etch pits in the center of the surface image. Simultaneously, the etch pits increase in depth as the dissolution reaction progresses. The movement of the steps and etch pit walls is directly related to the movement of the surface reactivity. At high simulation times, numerical errors occur in our simulation, leading to the formation of individual pits (**Fig. 9** 360 min). These pits have extreme slope values and thus accumulate the highest dissolution rates at the surface. The use of finer meshes reduces this effect and increases the maximum simulation time.

The rate spectrum remains similar for the first 3 h of dissolution time with the same shape as described in the previous section. This is consistent with the observations of the rate map, where the overall distribution remains similar and the highly reactive regions move only across the surface. For longer simulation times, the percentage of surface areas with rates >1 $\cdot 10^{-6}$ mol$\cdot$m$^{-2}\cdot$s^{-1} increases, while the surface areas with intermediate rates decrease. The percentage of surface area at high dissolution rates remains largely constant. This change in the rate spectrum is most likely associated with the development of pit spikes, where most of the surface tends toward lower dissolution rates. Apart from this effect, no changes in the dissolution rate spectrum were observed as dissolution progressed. The shape of the overall rate spectrum remained the same over time, with shifts between high- and low-reactive regions observed in the rate maps.

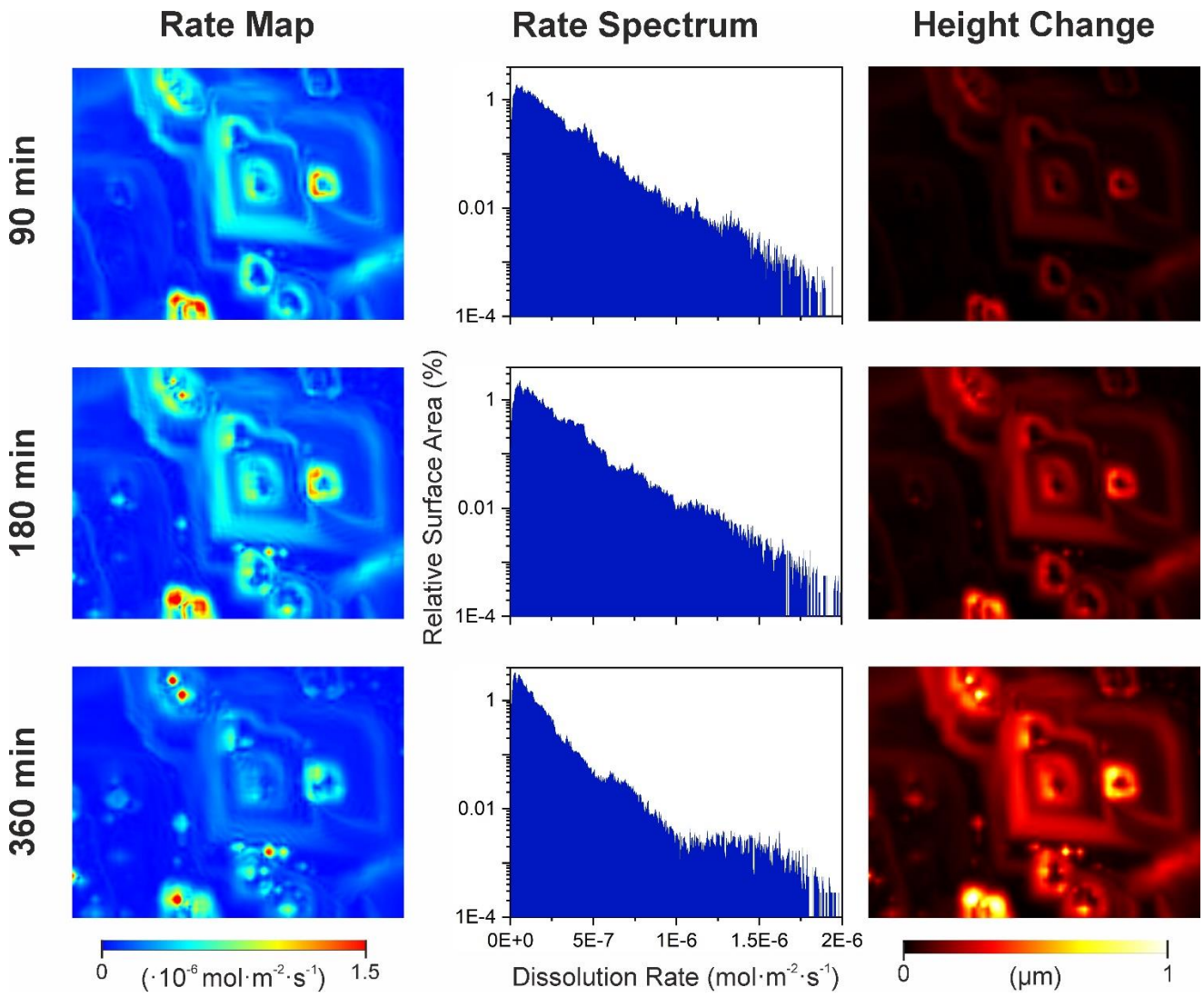

Figure 9: Evolution of the simulated system over 6 h of dissolution. The first column shows the rate maps after 90, 180, and 360 minutes. The second column shows all corresponding rate spectra (logarithmic y-axis). The third column shows the change in height accumulated over the reaction time. The dissolution rate distribution and spectra remain in a similar distribution during the first 180 minutes, with the reaction fronts moving outward from the pit center. After 180 minutes, individual pits develop with the highest reaction rates, while the largest sections of the surface transition to lower rates. The greatest height changes are observed at the etch pits, which widen and deepen as dissolution progresses.

3.4.2 Discussion

The temporal evolution of mineral dissolution and surface reactivity can be directly compared to the time series measured by Bibi et al. (2018). Some differences can be observed when comparing the rate maps. The experiment shows changes in the reactivity of the entire surface and also some specific surface areas over time. The average dissolution rate on the surface may increase and then decrease over time, with no pattern that can be deduced. The impact of surface structures can also change with time. Here, the central etch pit shows variations where the pit wall shows

high rates, but no consistent change over time. In contrast, our simulation results remain relatively constant over time with little changes due to the movement of the steps and thus reactivity on the surface. The agreement of the simulation with the experimental results varies depending on the interval chosen. This temporal behavior cannot currently be explained (Bibi et al., 2018), and our simulation does not reproduce this behavior, leading to the conclusion that the underlying mechanism is not yet included in the current reactivity distribution.

In other publications, the temporal evolution of the dissolution rates is investigated as well. Bollermann and Fischer (2020) did not observed a steady-state behavior of the dissolution rate for polycrystalline calcite. The overall surface normal retreat remained constant over the reaction period, while the local reactivity may change over time. In our simulation result, the overall rate spectrum remains mostly constant over the dissolution period without any significant changes. Fischer and Luttge (2018) described the pulsating behavior of surface reactivity at etch pit locations over time, resulting in multiple fronts that move outward from the pit as dissolution progresses. Our model predicts a similar step movement away from the etch pit center. However, no new reaction front is generated at the center of the pit, thus no pulsating behavior could be observed.

In general, the temporal behavior of dissolution rates and surface reactivity is poorly understood at present. Our model is not able to reproduce all currently available experimental results. It is therefore likely that the mechanisms involved have not been fully elucidated and are therefore not included in our reactivity parameterization. Further studies investigating the influence of time on dissolution reactions are needed to provide the basis for further improving the parametrization of the models.

3.5 Implications for larger 3D datasets

3.5.1 Results

To test the implementation of the SSF* in a 3D dataset consisting of multiple mineral grains, we developed a simple artificial pore geometry (**Fig. 10 A**). The geometry includes five inert quartz grains to create a heterogeneous flow field in the domain. Attached to the largest quartz crystal is a cuboidal calcite crystal that dissolves as the simulation time progresses. The front surface of the calcite crystal has the rough surface topography (**Fig. 1 A**), while the other four surfaces are entirely flat. The simulation uses the same geochemical, flow, and transport conditions as the previous 3D simulations (u = 1000 µm·s^{-}1, $D = 1 \cdot 10^{-9}$ m^2·s^{-1}) to induce calcite dissolution. Two simulations are performed and compared. In case (I), the classical rate equation without reactivity contribution is used, while case (II), the SSF* is included in the rate equation to describe the dissolution of the rough front surface.

In case (I), the highest dissolution rates are observed at the crystal edges and corners (**Fig. 10 C**). At these locations, the fluid flow passed the crystal and generates stronger velocity gradients with comparatively high fluid velocities close to the surface. This results in high local transport efficiency and increases the dissolution in comparison to the surfaces of the crystal. All five surfaces of the calcite crystal show constant, homogenous dissolution rates. The enclosed topography does not play a role in the dissolution of the frontal surface. Case (II), which includes the SSF* reactivity description, also shows the highest dissolution rates at the corners and edges (**Fig. 10 B**). The hydrodynamic conditions here are the same as in case (I), thus the same explanation applies. However, with proceeding dissolution, the edges become more rounded and consequently form areas with high slope values, which then continue to lead to high dissolution rates in later stages of the reaction. The lateral surfaces show the same behavior as in case (I), since they do not exhibit topography. In contrast, the frontal surface shows a strongly deviating rate distribution. The average dissolution rate is lower in comparison and the rates are not homogenously distributed. Even after 3 days of reaction time, the topography of the surface remains and influences the reactivity. Highly reactive areas are visible on the frontal surface (**Fig. 10 B**) and can be directly related to pit structures on the surface. The resolution of the structures in this model is relatively low compared to the previous simulations due to the overall larger system size and associated larger element size.

Figure 10 D compares the dissolution rate spectra of both cases after 3 days. In case (I), the minimum rate is 0.25 $\cdot 10^{-6}$ mol·m^{-2}·s^{-1}, while the flat crystal faces have rates between 0.3 $\cdot 10^{-6}$ mol·m^{-2}·s^{-1} and 0.8 $\cdot 10^{-6}$ mol·m^{-2}·s^{-1}. At higher rates, two main peaks are visible. The first peak

at 1.1 $\cdot 10^{-6}$ mol$\cdot$m$^{-2}\cdot$s^{-1} represents the surface areas close to the crystal edges where the rate increases due to the higher transport efficiency. At about 1.5 $\cdot 10^{-6}$ mol$\cdot$m$^{-2}\cdot$s^{-1}, the dissolution rates associated with the crystal edges and corners can be observed. A small high rate peak at 2 $\cdot 10^{-6}$ mol$\cdot$m$^{-2}\cdot$s^{-1} indicates the rate contribution of the vertices. In contrast, case (II) has large surface fractions with near-zero dissolution rate, which is due to the application of the SSF* on the front surface. On the front surface, increased dissolution rates due to surface reactivity contribute to the rate spectrum at about 0.4 $\cdot 10^{-6}$ mol$\cdot$m$^{-2}\cdot$s^{-1}. A second peak at 1.3 $\cdot 10^{-6}$ mol$\cdot$m$^{-2}\cdot$s^{-1} shows the high dissolution rates at the edges and corners.

Overall, two major differences can be observed between the classical and SSF* approaches. First, the surface topography does not play a role in the classical approach and will not change during the dissolution. In contrast, surface reactivity based on topography affects the rate distribution in the SSF* model. The heterogeneous rate distribution leads to changes in the surface topography and consequently to changes in the reactivity distribution over time. Second, the average dissolution rate of the calcite surface decreases when reactivity is included. Therefore, the evolution of the pore space over longer time periods will differ greatly between the two models.

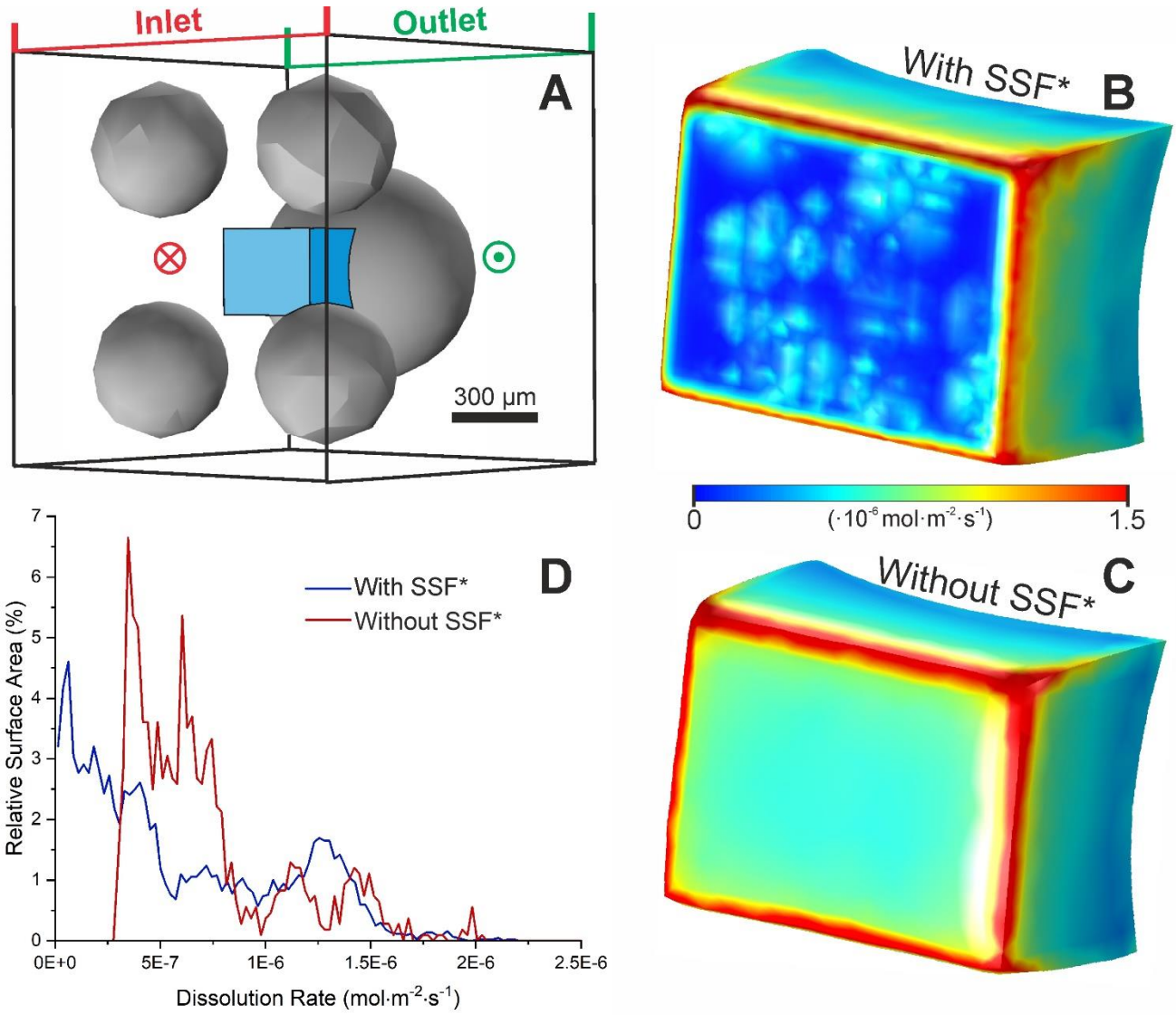

Figure 10: (A) Model sandstone with five inert quartz grains (grey spheres) and a calcite crystal (blue cuboid) located on the largest quartz grain. The calcite grain consists of four surfaces with no topography and one surface with the previously used topography dataset (opposite the quartz crystal). The inlet for flow is the left front boundary (red), and the outlet is at the opposite boundary (green). Calcite grain shape and dissolution rate distribution after 3 days of dissolution with (B) and without (C) the SSF* parameterization. (D) Dissolution rate spectra for the entire crystal surface.

3.5.2 Discussion

Both simulations predict that the strongest influence on the dissolution rate originates from the crystal corners and edges. This behavior has been observed previously in experiments on calcite single crystals (Noiriel and Soulaine, 2021; Noiriel et al., 2020; Noiriel et al., 2019). Noiriel and Soulaine (2021) discuss that some methods to compute dissolution rates from µ-CT datasets can lead to an overestimation at the edges of the crystal sample. In our model, the dissolution rates are first calculated based on chemical and reactivity conditions, and then lead to a corresponding

decrease in height. The process is thus reversed compared to the experimental path and a high dissolution rate cannot be due to this effect.

In case (I), the high rates at edges and corners can be caused exclusively by hydrodynamic conditions and are not related to intrinsic crystal reactivity. Increased reactivity was found at edges and corners due to the high concentration of kink sites at these surface features (Bollermann and Fischer, 2020; Noiriel et al., 2019). **Figure 11** shows a schematic overview of the crystal surface and explains the heterogeneous reactivity at flat surfaces, etch pits and edges. The increased edge reactivity can be captured with the slope parameterization, as the rounded edges exhibit an increased slope in comparison to the flatter surfaces they connect. Due to their inherent reactivity, the highest rates remain at the edges. In contrast, the crystal surfaces have, on average, lower concentrations of reactive sites and therefore lower dissolution rates.

This difference is visible in case (II) and is similar to the measurement of Noiriel et al. (2019). The main cause of high dissolution rates on the surface are etch pits that open up as the reaction time progresses and consequently produce large steps of high reactivity that move across the surface in both simulation and experiment (Noiriel et al., 2019). This behavior cannot be reproduced with the classical rate equation, where the structures of the surface topography do not play any role in the dissolution reaction. Therefore, such a model introduces errors in predicting the evolution of the fluid-mineral interface over time, which can affect surface-sensitive processes such as the adsorption of species onto the surface. It may also affect the evolution of pore geometries in natural rock systems in terms of parameters such as shape and connectivity.

The overall lower dissolution rates when SSF* is included also result in a slower volume loss of the crystal (**Fig. S1** in the Supporting Information). After three days, the difference between the two cases is about 2% of the initial volume, and the difference increases with time. This can lead to large differences in simulations on long time scales. A linear extrapolation of the volume loss in our two cases shows that crystal reaches half of its volume after 340 days without SSF* parameterization, while it requires 420 days when the SSF* is included. Large differences in predicted dissolved volume affect the available pore space, pore geometries, and permeability of the simulated rock sample. This can be illustrated by a simple calculation based on a sandstone with 15% calcite cement and 2% porosity described by Heidsiek et al. (2020). Using our simple volume loss extrapolation, the porosity of the sandstone increases after 340 days to 9.5% without the SSF* and to 7.9% with the SSF* parameterization. The difference in predicted porosity is 1.5%, which may have a significant effect on the hydrodynamic conditions in the sandstone, especially for permeability-determining volumes at pore throats. A precise description of the pore structures is needed to model and predict the evolution of geological environments as they play a critical role

in controlling the physical properties and processes in the rock (Anovitz and Cole, 2015). Therefore, to achieve an accurate prediction of future hydrodynamic conditions in the rock, a precise approximation of mineral surface reactivity is required.

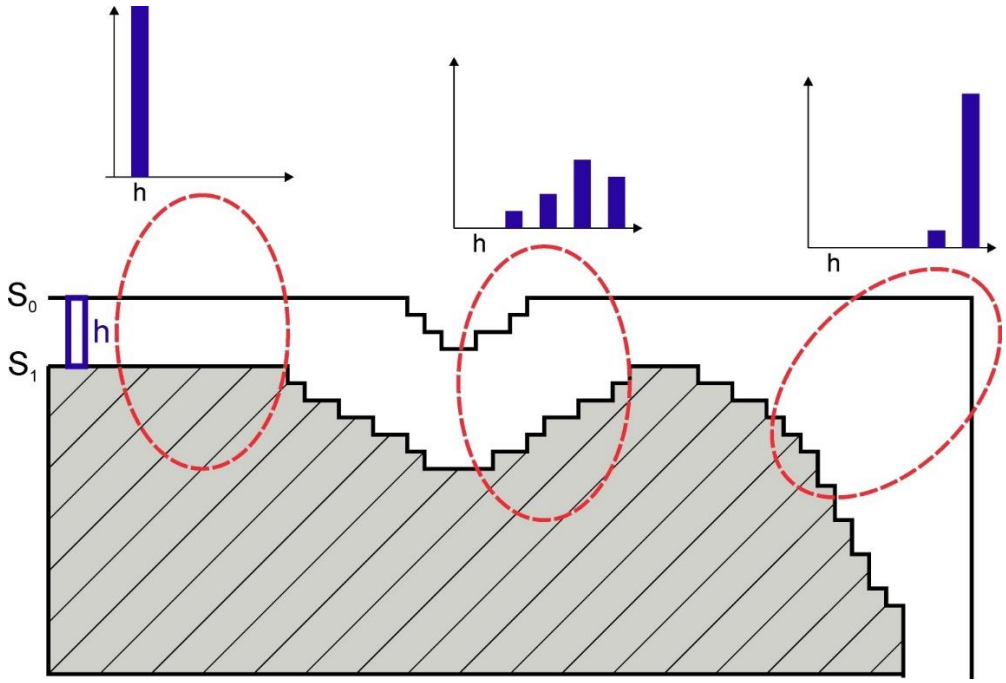

Figure 11: Schematic representation of the crystal surface before (S_0) and after (S_1) dissolution. Exemplary rate spectra based on block removal are shown for specific surface sections, including a flat area, an etch pit wall, and the crystal corner. The flat surface shows only the general height retreat and an uniform dissolution rate. At the etch pit, more blocks are removed due to the higher reactivity at the steps. Thus, the dissolution rates increase and show a more heterogonous pattern due to differences in the concentration and rate of the reactive sites. The crystal corner has the highest concentration of reactive sites. Here, the most material is removed, resulting in the highest observed dissolution rates.

5. Summary and conclusions

We have confirmed the conclusion from previous publications that the current rate equation approach in pore-scale reactive transport models cannot reproduce the experimentally derived dissolution rates for mineral surfaces (Agrawal et al., 2021; Karimzadeh and Fischer, 2021). Surface reactivity is a material-inherent parameter that needs to be considered, especially for surface controlled transport conditions. Based on the approach by Karimzadeh and Fischer (2021) to use the surface slope as an approximation for first-order reactivity, we further improved the rate equation based on the surface slope parametrization. The improved SSF* can be applied to datasets with a larger field of view, larger height variation, and longer reaction times. The SSF* approach significantly improves the agreement between model and experimental results with respect to the components of the dissolution rate spectrum. This improved fit increases the predictive capabilities of reactive transport models regarding porosity and permeability evolution of natural rock samples. Our parameterization can be applied to pore network scale simulations, e.g., derived from µ-CT datasets. The parameter can be applied to any mineral by fitting the SSF* normalization to the respective experimental rate spectra. Once an SSF* normalization is derived, it can be used for any future simulation with surfaces of the same mineral. In this study, we have shown a pathway to incorporate a first-order approximation for surface reactivity into large pore-scale models to obtain an accurate description of the mineral dissolution and thus the evolution of the pore network, flow field, and permeability.

Acknowledgments

The authors thank Tao Yuan for fruitful discussions on the design of the reactive transport models and interpretation of the results. We thank the German Federal Ministry of Education and Research (grant 02NUK053) and the Helmholtz Association (grant SO-093; iCross) for funding.

Research Data

Research Data associated with this article can be accessed at https://rodare.hzdr.de/.

References

Agrawal P., Raoof A., Iliev O. and Wolthers M. (2020) Evolution of pore-shape and its impact on pore conductivity during CO2 injection in calcite: Single pore simulations and microfluidic experiments. *Adv Water Resour* **136**, 103480.

Agrawal P., Bollermann T., Raoof A., Iliev O., Fischer C. and Wolthers M. (2021) The contribution of hydrodynamic processes to calcite dissolution rates and rate spectra. *Geochim. Cosmochim. Acta* **307**, 338-350.

Amelinckx S., Bontinck W. and Dekeyser W. (1957) Helical Dislocations and Spiral Etch-Pits. *Philos. Mag.* **2**, 1264-1270.

Anovitz L. M. and Cole D. R. (2015) Characterization and Analysis of Porosity and Pore Structures. *Rev Mineral Geochem* **80**, 61-164.

Arvidson R. S., Ertan I. E., Amonette J. E. and Luttge A. (2003) Variation in calcite dissolution rates. *Geochim. Cosmochim. Acta* **67**, 1623-1634.

Berkowitz B. (2002) Characterizing flow and transport in fractured geological media: A review. *Adv Water Resour* **25**, 861-884.

Bibi I., Arvidson R., Fischer C. and Lüttge A. (2018) Temporal Evolution of Calcite Surface Dissolution Kinetics. *Minerals* **8**, 256.

Blunt M. J., Bijeljic B., Dong H., Gharbi O., Iglauer S., Mostaghimi P., Paluszny A. and Pentland C. (2013) Pore-scale imaging and modelling. *Adv Water Resour* **51**, 197-216.

Bollermann T. and Fischer C. (2020) Temporal evolution of dissolution kinetics of polycrystalline calcite. *Am. J. Sci.* **320**, 53-71.

Bouissonnié A., Daval D., Marinoni M. and Ackerer P. (2018) From mixed flow reactor to column experiments and modeling: Upscaling of calcite dissolution rate. *Chem. Geol.* **487**, 63-75.

Busenberg E., Plummer L. and Mumpton F. (1986) A comparative study of the dissolution and crystal growth kinetics of calcite and aragonite. *Studies Diagenesis USGS Bull* **1578**, 139-168.

Chen J. C., Reischl B., Spijker P., Holmberg N., Laasonen K. and Foster A. S. (2014) Ab initio Kinetic Monte Carlo simulations of dissolution at the NaCl-water interface. *Phys. Chem. Chem. Phys.* **16**, 22545-22554.

Cheng V. K. W. and Coller B. A. W. (1987) Monte Carlo simulation study on the dissolution of a train of infinitely straight steps and of an infinitely straight crystal edge. *J. Cryst. Growth* **84**, 436-454.

Chou L., Garrels R. M. and Wollast R. (1989) Comparative study of the kinetics and mechanisms of dissolution of carbonate minerals. *Chem. Geol.* **78**, 269-282.

Deng H., Molins S., Trebotich D., Steefel C. and DePaolo D. (2018) Pore-scale numerical investigation of the impacts of surface roughness: Upscaling of reaction rates in rough fractures. *Geochim. Cosmochim. Acta* **239**, 374-389.

Druhan J. and Tournassat C. (2020) *Reactive Transport in Natural and Engineered Systems*. De Gruyter, Berlin, Boston.

Ewing R. C., Whittleston R. A. and Yardley B. W. D. (2016) Geological Disposal of Nuclear Waste: a Primer. *Elements* **12**, 233-237.

Fischer C. and Luttge A. (2018) Pulsating dissolution of crystalline matter. *Proc. Natl. Acad. Sci. U.S.A.* **115**, 897-902.

Fischer C., Arvidson R. S. and Lüttge A. (2012) How predictable are dissolution rates of crystalline material? *Geochim. Cosmochim. Acta* **98**, 177-185.

Fischer C., Kurganskaya I. and Luttge A. (2018) Inherited control of crystal surface reactivity. *Appl. Geochem.* **91**, 140-148.

Fischer C., Kurganskaya I., Schäfer T. and Lüttge A. (2014) Variability of crystal surface reactivity: What do we know? *Appl. Geochem.* **43**, 132-157.

Harb J. N. and Alkire R. C. (1989) The effect of fluid flow on growth of single corrosion pits. *Corros. Sci.* **29**, 31-43.

Heidsiek M., Butscher C., Blum P. and Fischer C. (2020) Small-scale diagenetic facies heterogeneity controls porosity and permeability pattern in reservoir sandstones. *Environ. Earth Sci.* **79**, 425.

Higdon J. J. (1985) Stokes flow in arbitrary two-dimensional domains: shear flow over ridges and cavities. *J. Fluid Mech.* **159**, 195-226.

Kahl W.-A., Yuan T., Bollermann T., Bach W. and Fischer C. (2020) Crystal surface reactivity analysis using a combined approach of X-ray micro-computed tomography and vertical scanning interferometry. *Am. J. Sci.* **320**, 27-52.

Karimzadeh L. and Fischer C. (2021) Implementing Heterogeneous Crystal Surface Reactivity in Reactive Transport Simulations: The Example of Calcite Dissolution. *ACS Earth Space Chem.* **5**, 2408-2418.

Kurganskaya I. and Luttge A. (2013) Kinetic Monte Carlo Simulations of Silicate Dissolution: Model Complexity and Parametrization. *J. Phys. Chem. C* **117**, 24894-24906.

Kurganskaya I. and Luttge A. (2016) Kinetic Monte Carlo Approach To Study Carbonate Dissolution. *J. Phys. Chem. C* **120**, 6482-6492.

Kurganskaya I., Arvidson R. S., Fischer C. and Luttge A. (2012) Does the stepwave model predict mica dissolution kinetics? *Geochim. Cosmochim. Acta* **97**, 120-130.

Lange I., Toro M., Arvidson R. S., Kurganskaya I. and Luttge A. (2021) The role of crystal heterogeneity in alkali feldspar dissolution kinetics. *Geochim. Cosmochim. Acta* **309**, 329-351.

Lasaga A. C. and Lüttge A. (2003) A model for crystal dissolution. *Eur. J. Mineral.* **15**, 603-615.

Liang Y. and Baer D. (1997) Anisotropic dissolution at the CaCO3 (10$\bar{1}$4)—water interface. *Surf. Sci.* **373**, 275-287.

Luttge A., Arvidson R. S. and Fischer C. (2013) A Stochastic Treatment of Crystal Dissolution Kinetics. *Elements* **9**, 183-188.

Martin P., Gaitero J. J., Dolado J. S. and Manzano H. (2020) KIMERA: A Kinetic Montecarlo Code for Mineral Dissolution. *Minerals* **10**, 825.

Menke H. P., Bijeljic B. and Blunt M. J. (2017) Dynamic reservoir-condition microtomography of reactive transport in complex carbonates: Effect of initial pore structure and initial brine pH. *Geochim. Cosmochim. Acta* **204**, 267-285.

Menke H. P., Andrew M. G., Blunt M. J. and Bijeljic B. (2016) Reservoir condition imaging of reactive transport in heterogeneous carbonates using fast synchrotron tomography — Effect of initial pore structure and flow conditions. *Chem. Geol.* **428**, 15-26.

Molins S., Trebotich D., Yang L., Ajo-Franklin J. B., Ligocki T. J., Shen C. and Steefel C. I. (2014) Pore-scale controls on calcite dissolution rates from flow-through laboratory and numerical experiments. *Environ. Sci. Technol.* **48**, 7453-7460.

Molins S., Soulaine C., Prasianakis N. I., Abbasi A., Poncet P., Ladd A. J. C., Starchenko V., Roman S., Trebotich D., Tchelepi H. A. and Steefel C. I. (2021) Simulation of mineral dissolution at the pore scale with evolving fluid-solid interfaces: review of approaches and benchmark problem set. *Comput. Geosci.* **25**, 1285-1318.

Noiriel C. and Daval D. (2017) Pore-Scale Geochemical Reactivity Associated with CO2 Storage: New Frontiers at the Fluid–Solid Interface. *Accounts of Chemical Research* **50**, 759-768.

Noiriel C. and Soulaine C. (2021) Pore-Scale Imaging and Modelling of Reactive Flow in Evolving Porous Media: Tracking the Dynamics of the Fluid-Rock Interface. *Transp Porous Media* **140**, 181-213.

Noiriel C., Oursin M. and Daval D. (2020) Examination of crystal dissolution in 3D: A way to reconcile dissolution rates in the laboratory? *Geochim. Cosmochim. Acta* **273**, 1-25.

Noiriel C., Oursin M., Saldi G. and Haberthur D. (2019) Direct Determination of Dissolution Rates at Crystal Surfaces Using 3D X-ray Microtomography. *ACS Earth Space Chem.* **3**, 100-108.

Pereira Nunes J. P., Blunt M. J. and Bijeljic B. (2016a) Pore-scale simulation of carbonate dissolution in micro-CT images. *J. Geophys. Res. Solid Earth* **121**, 558-576.
Pereira Nunes J. P., Bijeljic B. and Blunt M. J. (2016b) Pore-space structure and average dissolution rates: A simulation study. *Water Resour. Res.* **52**, 7198-7212.
Plummer L., Wigley T. and Parkhurst D. (1978) The kinetics of calcite dissolution in CO 2-water systems at 5 degrees to 60 degrees C and 0.0 to 1.0 atm CO 2. *Am. J. Sci.* **278**, 179-216.
Pokrovsky O. S., Golubev S. V. and Schott J. (2005) Dissolution kinetics of calcite, dolomite and magnesite at 25 °C and 0 to 50 atm pCO2. *Chem. Geol.* **217**, 239-255.
Pollet-Villard M., Daval D., Fritz B., Knauss K. G., Schäfer G. and Ackerer P. (2016) Influence of etch pit development on the surface area and dissolution kinetics of the orthoclase (001) surface. *Chem. Geol.* **447**, 79-92.
Prasianakis N. I., Curti E., Kosakowski G., Poonoosamy J. and Churakov S. V. (2017) Deciphering pore-level precipitation mechanisms. *Scientific Reports* **7**, 13765.
Rasoulzadeh M., Yekta A., Deng H. and B. Ghahfarokhi R. (2020) Semi-analytical models of mineral dissolution in rough fractures with permeable walls. *Phys. Fluids* **32**, 052003.
Rohlfs R., Fischer C., Kurganskaya I. and Luttge A. (2018) Crystal Dissolution Kinetics Studied by a Combination of Monte Carlo and Voronoi Methods. *Minerals* **8**, 133.
Saldi G. D., Voltolini M. and Knauss K. G. (2017) Effects of surface orientation, fluid chemistry and mechanical polishing on the variability of dolomite dissolution rates. *Geochim. Cosmochim. Acta* **206**, 94-111.
Schwoebel R. L. and Shipsey E. J. (1966) Step Motion on Crystal Surfaces. *J. Appl. Phys.* **37**, 3682-3686.
Shao H., Dmytrieva S. V., Kolditz O., Kulik D. A., Pfingsten W. and Kosakowski G. (2009) Modeling reactive transport in non-ideal aqueous–solid solution system. *Appl. Geochem.* **24**, 1287-1300.
Steefel C. I., Appelo C. A. J., Arora B., Jacques D., Kalbacher T., Kolditz O., Lagneau V., Lichtner P. C., Mayer K. U., Meeussen J. C. L., Molins S., Moulton D., Shao H., Šimůnek J., Spycher N., Yabusaki S. B. and Yeh G. T. (2015) Reactive transport codes for subsurface environmental simulation. *Comput. Geosci.* **19**, 445-478.
Tournassat C. and Steefel C. I. (2019) Reactive Transport Modeling of Coupled Processes in Nanoporous Media. *Rev Mineral Geochem* **85**, 75-109.
Wolthers M., Charlet L. and Van Cappellen P. (2008) The surface chemistry of divalent metal carbonate minerals; a critical assessment of surface charge and potential data using the charge distribution multi-site ion complexation model. *Am. J. Sci.* **308**, 905-941.
Yuan T., Ning Y. and Qin G. (2016) Numerical Modeling and Simulation of Coupled Processes of Mineral Dissolution and Fluid Flow in Fractured Carbonate Formations. *Transp Porous Media* **114**, 747-775.
Zhang L. and Lüttge A. (2009) Theoretical approach to evaluating plagioclase dissolution mechanisms. *Geochim. Cosmochim. Acta* **73**, 2832-2849.
Zou L., Jing L. and Cvetkovic V. (2017) Modeling of Solute Transport in a 3D Rough-Walled Fracture–Matrix System. *Transp Porous Media* **116**, 1005-1029.